

Some Applications of Phase-Field Approaches to
Fracture (Need to somehow mention variational
frameworks and nonlinearity)

by

Tianchen Hu

Department of Mechanical Engineering and Materials Science
Duke University

Date: _____

Approved:

John Dolbow, Advisor

Wilkins Aquino

Johann Guilleminot

Manolis Veveakis

Benjamin W. Spencer

Dissertation submitted in partial fulfillment of the requirements for the degree of
Doctor of Philosophy in the Department of Mechanical Engineering and Materials
Science
in the Graduate School of Duke University
2021

ABSTRACT

Some Applications of Phase-Field Approaches to Fracture
(Need to somehow mention variational frameworks and
nonlinearity)

by

Tianchen Hu

Department of Mechanical Engineering and Materials Science
Duke University

Date: _____
Approved:

John Dolbow, Advisor

Wilkins Aquino

Johann Guilleminot

Manolis Veveakis

Benjamin W. Spencer

An abstract of a dissertation submitted in partial fulfillment of the requirements for
the degree of Doctor of Philosophy in the Department of Mechanical Engineering
and Materials Science
in the Graduate School of Duke University
2021

Copyright © 2021 by Tianchen Hu
All rights reserved

Abstract

Lorem ipsum dolor sit amet, consectetur adipiscing elit. Sed porta finibus lacus venenatis varius. Proin luctus, est ac facilisis aliquam, leo est tempus velit, eu euismod mi nunc ut odio. Nulla porttitor velit vel dolor dapibus sollicitudin. Sed lobortis lorem ut dui bibendum pellentesque. Curabitur in volutpat ex, ut semper ipsum. In auctor ac ex euismod aliquet. Ut rutrum neque sed felis auctor luctus. Mauris nec lorem placerat, mattis turpis vel, lacinia purus. Maecenas nunc mauris, semper ut aliquam at, luctus sed justo. Proin porttitor cursus orci. Ut id vehicula massa, ac sagittis lectus. Sed eget justo faucibus, posuere purus.

Contents

Abstract	iv
List of Tables	viii
List of Figures	ix
Acknowledgements	xiii
1 Introduction	1
1.1 Background	1
1.2 Organization of the dissertation	1
1.3 Notation	1
2 The Variational Framework	3
2.1 Kinematics and Constraints	3
2.2 Thermodynamics	4
2.2.1 Thermodynamics	4
2.3 The minimization problem	6
2.4 Discretization	6
3 Brittle Fracture: Fracture in Microstructures	7
3.1 Introduction	7
3.2 Theory	7
3.2.1 Constitutive choices	7
3.2.2 Approximation of the pressure boundary condition	7

3.3	Verification	7
3.3.1	Uniaxial traction of a bar	7
3.3.2	Pressurized crack propagation	7
3.4	Numerical examples	7
3.4.1	Effects of pore geometry, porosity, and loading conditions	7
3.4.2	High burnup structure fragmentation	7
4	Cohesive Fracture: Soil Dessication	8
4.1	Introduction	8
4.2	Theory	13
4.2.1	Constitutive choices	13
4.2.2	Enforcing the traction-free boundary condition	15
4.2.3	Stochastic models for fracture properties	18
4.3	Verification	26
4.3.1	Mode I: Edge-Notched Unilateral Tension Test	26
4.3.2	Mode II: Edge-Notched Shear Test	29
4.3.3	Crack Propagation Under Biaxial Tension	32
4.3.4	Reconstruction of the marginal PDF	36
4.4	Numerical examples	36
4.4.1	One-Dimensional Simplification: Side View	36
4.4.2	Two-Dimensional Simplification: Stochastic Aspects of Fracture	40
4.4.3	Inverse Identification Based on Three-Dimensional Physical Experiments	52
5	Towards Ductile Fracture	58
5.1	Introduction	58
5.2	Theory	58
5.2.1	Constitutive choices	58

5.2.2	A power-law approximation to the yield surface	58
5.2.3	Variational constitutive updates	58
5.3	Verification	58
5.3.1	A homogeneous example: uniaxial constitutive response	58
5.3.2	A nonhomogeneous example: uniaxial load-displacement curves	58
5.3.3	Crack resistance curves	58
5.4	Numerical examples	58
5.4.1	Three-point bending	58
5.4.2	The Sandia Fracture Challange	58
5.4.3	Spallation of oxidation scale	58
6	Conclusion	59
A	Code availability	60
B	On the phase-field irreversibility constraint	61
C	The flooding algorithm for counting fragments	62
	Bibliography	66
	Biography	72

List of Tables

4.1	Summary of material properties and model parameters for all calculations in ??	41
4.2	Summary of material properties of mining waste and model parameters for all calculations in ??	53
C.1	Demonstration of classification after the update from time step n to time step n+1. Broken elements are denoted with an underscore.	65

List of Figures

4.1	Boundary conditions of the plate with a pre-existing crack for (a) a mode I tension test and (d) a mode II shear test. Finite element meshes for the mode I calculations (b - c) and for the mode II calculations (e - f). For (b, e) the meshes have the initial crack geometry “meshed-in” while (c, f) have local refinement around the initial damage field. All meshes are pre-refined along the predicted crack-path with a characteristic element size of 0.005 mm.	28
4.2	Edge-notched specimen loaded in tension with initial crack represented by a geometric notch with a rounded corner. (a) Dimensions of the notched plate. Damage d at (b) $u_y = 0$ mm, (c) $u_y = 0.0048$ mm, (d) $u_y = 0.006$ mm.	28
4.3	Edge-notched specimen loaded in tension with initial crack represented by a damage field. (a) Dimensions of the intact plate. The Damage d at (b) $u_y = 0$ mm (c) $u_y = 0.0048$ mm (d) $u_y = 0.006$ mm.	29
4.4	Mode I force-displacement curves obtained using (a) the spectral decomposition with two representations of the pre-existing crack (b) a spectral decomposition in conjunction with the contact split with different critical damage threshold on two representations of the pre-existing crack.	30
4.5	The crack paths obtained using (a-d) the spectral decomposition on a geometrically notched plate, (e-h) the spectral decomposition with an initial damage field d_0 (4.53) representing the initial crack, and (i-l) the contact split with an initial damage field. Snapshots of crack paths are shown at (b,f,j) $u_x = 0$ mm, (c,g,k) $u_x = 0.0109$ mm, and (d,h,l) $u_x = 0.02$ mm.	31
4.6	Mode II force-displacement curves obtained using (a) spectral decomposition with two representations of the initial crack (b) spectral decomposition in conjunction with the contact split with different critical damage threshold on two representations of the initial crack.	32

4.7	(a) Dimensions and boundary conditions of a thin plate with two parallel initial cracks. (b) The initial cracks are represented by an initial damage field.	34
4.8	Crack paths obtained using (a-c) a no-split technique (d-f) the spectral decomposition (g-i) the contact split.	35
4.9	Contour plot of the normal pressure right before the bridge forms. The pressure is calculated for an orientation that is estimated to be orthogonal to the bridge. Elements within the contour of $d = 0.75$ are removed to indicate the current crack set.	36
4.10	Description of a one-dimensional model for thin-film cracking. (a) Side view (highlighted in yellow) of the geometry (b) schematic representation of the side view. The elasticity solution is derived for the region highlighted with the shaded box, i.e. between the two discontinuities across the thin film. The coordinate system is centered at the middle of the bottom surface of the thin film.	37
4.11	The principal of “super-superposition” applied to the region of interest marked in Figure 4.10b. The analytical solution is derived based on the boundary conditions shown in (c).	37
4.12	Relationship between the dimensionless fracture driving energy and the dimensionless crack spacing: (a) analytical solution using linear elasticity; and (b) numerically generated curves using the phase-field for cohesive model detailed in this work.	40
4.13	Description of a two-dimensional model for thin-film cracking. (a) Top view (highlighted in yellow) (b) schematic representation of the top view. A typical crack is shown to emphasize that fracture is only considered in the film.	42
4.14	Damage fields resulting from six pairs of realizations with different correlation models and normalized correlation lengths. The left three pairs (a-b, g-h, m-n) are realizations obtained with a PSE covariance function, while the right three pairs (d-e, j-k, p-q) are samples generated with a PE covariance function. Energy release rate \mathcal{G}_c and the critical fracture energy ψ_c have a coefficient of variation of 0.03, and normalized spatial correlation length L^* of (a-b, d-e) 0.05 (g-h, j-k) 0.1 (m-n, p-q) 0.2 The corresponding damage fields are shown in (c, f, i, l, o, r), respectively. In these results, independent realizations of the underlying Gaussian fields are used.	45

4.15 Three pairs of qualitative comparison of smoothness of the kernel function with the same normalized correlation length $L^* = 0.05$. (a-f) pair 1 (g-l) pair 2 (m-r) pair 3. Each row compares two kernel functions transformed from the same samples of the underlying Gaussian fields.	46
4.16 (a, c) Mean dimensionless crack spacing \underline{l}^* versus dimensionless crack driving force \mathcal{D}^* (b, d) Estimated probability density of dimensionless crack spacing for different values of correlation length when $\mathcal{D}^* = 5.17$ based on (a-b) a PSE kernel (c-d) a PE kernel	47
4.17 Comparisons of (a) mean dimensionless crack spacing \underline{l}^* versus dimensionless crack driving force \mathcal{D}^* and (b) Estimated probability density of dimensionless crack spacing for different values of correlation length when $\mathcal{D}^* = 5.17$ for results obtained using a PSE kernel and a PE kernel	48
4.18 Point-wise correlated material properties: (a-f) normalized fracture toughness \mathcal{G}_c^* and (g-l) normalized critical fracture energy ψ_c^* with (left) PSE covariance function (right) PE covariance function	49
4.19 Comparisons of (a) mean dimensionless crack spacing as a function of dimensionless crack driving force and (b) estimated PDFs of dimensionless fragment size at loading $\mathcal{D}^* = 5.17$ for results with an underlying PSE kernel	49
4.20 Comparisons of (a) mean dimensionless crack spacing and dimensionless crack driving force and (b) estimated PDFs of dimensionless fragment size at loading $\mathcal{D}^* = 5.17$ for results with an underlying PE kernel	50
4.21 Superposition of fracture networks obtained by three samples of different coefficients of correlation, using the PSE kernel. Only the volume within the damage contour of $d = 0.9$ is shown to represent the resulting fracture network. Three samples are sampled (a) by holding \mathcal{G}_c constant and (b) by holding ψ_c constant.	51
4.22 Snapshots of damage field at different loading levels with $d \geq 0.75$ plotted over (a-c) fracture toughness \mathcal{G}_c and (d-f) critical fracture energy ψ_c with an underlying PSE covariance function	52
4.23 Snapshots of damage field at different loading levels with $d \geq 0.75$ plotted over (a-c) fracture toughness \mathcal{G}_c and (d-f) critical fracture energy ψ_c with an underlying PE covariance function	53

4.24 Three sets of experiments and calculations for (a-e) unilateral agitation (f-j) rotational agitation (k-o) point agitation. (b, g, l) snapshots of crack patterns from experiments. postulated spatially correlated (c, h, m) fracture toughness and (d, i, n) critical fracture energy to reproduce experimental observations. (e, j, o) damage fields obtained using corresponding spatially varying material properties.	54
4.25 Procedures of finding the optimal hyperparameter to match the experiment: (a) 12 pairs of fracture properties are sampled to explore the space of admissible spatial correlation lengths; three dimensional energy minimization problems are solved to obtain (b) the resulting fracture morphology; (c) distributions of fragment sizes are extracted from the simulated results, and the log-likelihood values of these distributions at the samples extracted from (d) the experimental fracture morphology are computed.	55
4.26 (a) Estimated PDFs of the dimensionless fragment sizes extracted from the experimental result and the calibrated stochastic model. (b) Fracture morphology obtained using the calibrated fracture properties. (c) Photograph of cracks in the mining waste.	56
4.27 Qualitative comparison between the experiments and the simulations: (a-c) Photographs (modified from [1]) of cracks in mining waste due to desiccation at steady state for three test specimens with thickness (a) 4 mm, (b) 8 mm, and (c) 16 mm. (d-f) Top view and (g-i) panoramic view of corresponding numerical simulation results with different film thickness. Volumes of material with $d \geq 0.75$ were removed to improve the visualization of the crack geometry.	57
C.1 (a) Final damage field obtained using a spatially correlated random \mathcal{G}_c and ψ_c . (b) Corresponding clusters labeled by the flooding algorithm. Cluster boundaries are marked in black.	63
C.2 Status change from step n to step n+1. “Broken” elements are labeled in yellow, and “intact” elements are white. The step-by-step reclassification procedure is shown in Table C.1.	65

Acknowledgements

I am thankful for the many people.

1

Introduction

Introduction placeholder.

1.1 Background

1.2 Organization of the dissertation

1.3 Notation

In what follows, deterministic scalar, vectors, second-order tensors, and fourth-order tensors are denoted by a (or A), \mathbf{a} (or \mathbf{A}), \mathbf{A} , and \mathbb{A} , respectively.

Let Ω be a collection of points $\mathbf{X} \in \mathbb{R}^d$, $d \in \{1, 2, 3\}$. Scalar- and vector-valued random fields defined on the probability space $(\Theta, \Sigma, \mathbb{P})$, indexed by Ω , are denoted as $\{A(\mathbf{X}), \mathbf{X} \in \Omega\}$ and $\{\mathbf{A}(\mathbf{X}), \mathbf{X} \in \Omega\}$, respectively. At any fixed material point $\mathbf{X} \in \Omega$, $a(\mathbf{X})$ and $\mathbf{a}(\mathbf{X})$ are random variables defined on the probability space $(\Theta, \Sigma, \mathbb{P})$. For any fixed $\theta \in \Theta$, $a(\theta)$ and $\mathbf{a}(\theta)$ are realizations of the random variables. Similarly, $\mathbf{X} \mapsto a(\mathbf{X}; \theta)$ and $\mathbf{X} \mapsto \mathbf{a}(\mathbf{X}; \theta)$ are realizations of the random fields $\{A(\mathbf{X}), \mathbf{X} \in \Omega\}$ and $\{\mathbf{A}(\mathbf{X}), \mathbf{X} \in \Omega\}$.

Einstein summations are assumed wherever applicable unless otherwise stated.

For any vectors \mathbf{a} and \mathbf{b} of the same size, the inner product is defined as $\mathbf{a} \cdot \mathbf{b} = a_i b_i$ where a_i and b_i are components of the vectors. The associated vector norm is $\|\mathbf{a}\|^2 = a \cdot a$. Similarly, for any second-order tensors \mathbf{A} and \mathbf{B} of the same size, the inner product is defined as $\mathbf{A} : \mathbf{B} = \text{tr}(\mathbf{A}^T \mathbf{B})$. The associated Frobenius norm writes $\|\mathbf{A}\|_F = \sqrt{\mathbf{A} : \mathbf{A}}$.

2

The Variational Framework

2.1 Kinematics and Constraints

We start by defining degrees of freedom in the system. Let Ω be a body consisting of a continuous collection of material points. Let $\Omega_0 \subset \mathbb{R}^d$ be the reference configuration at some time $t = t_0$, whose particles are identified by their position \mathbf{X} , and Ω_t be the current configuration at time $t > t_0$, with particles at position \mathbf{x} . Let $\Phi : \mathbf{X} \mapsto \mathbf{x}$ be the deformation map from $\mathbf{X} \in \Omega_0$ to $\mathbf{x} \in \Omega_t$. The deformation gradient is denoted as $\mathbf{F} = \nabla \Phi$, where the operator ∇ denotes differentiation with respect to \mathbf{X} . The Jacobian determinant of the deformation gradient is defined as $J = \det \mathbf{F}$. Plastic (creep) deformations are modeled through the framework of multiplicative decomposition

$$\mathbf{F} = \mathbf{F}^e \mathbf{F}^p \mathbf{F}^g, \quad (2.1)$$

where \mathbf{F}^e , \mathbf{F}^p are referred to as the elastic and plastic deformation gradients, respectively. \mathbf{F}^g is the product of eigen deformation gradients. For example, isotropic thermal expansion can be accounted by $\mathbf{F}^g = (1 + \alpha \Delta T) \mathbf{I}$, where α is the thermal expansion coefficient, and T is the temperature. In general, the plastic distortion

evolves subject to constraints of the following form

$$\mathcal{Z}(\dot{\mathbf{F}}^p \mathbf{F}^{p-1}, \dot{\bar{\varepsilon}}^p) = 0, \quad (2.2)$$

where $\bar{\varepsilon}^p$ is the effective plastic strain.

Crack surfaces are regularized and modeled using a phase-field d , $0 \leq d \leq 1$, where $d = 0$ represents the intact state of a material point, and $d = 1$ indicates the material point has lost all of its load-carrying capacity.

Both the plastic distortion and the fracture evolution are considered irreversible, i.e.

$$\dot{\bar{\varepsilon}}^p \geq 0, \quad \dot{d} \geq 0. \quad (2.3)$$

The collected set of kinematic degrees of freedom are

$$\mathcal{K} = \{\boldsymbol{\Phi}, \mathbf{F}^p, \bar{\varepsilon}^p, d\}, \quad (2.4)$$

and the thermodynamic and caloric states of the system are characterized by the temperature T and the kinematics \mathcal{K} .

2.2 Thermodynamics

2.2.1 Thermodynamics

The rates of change of the kinematic variables are denoted as $\mathcal{V} = \{\dot{\boldsymbol{\Phi}}, \dot{\mathbf{F}}^p, \dot{\bar{\varepsilon}}^p, \dot{d}\}$. The generalized velocities of the kinematic state variables and their corresponding thermodynamic force conjugates are collected in the sets

$$\dot{\Lambda} = \{\nabla \dot{\boldsymbol{\Phi}}, \dot{\mathbf{F}}^p, \dot{\bar{\varepsilon}}^p, \dot{d}, \nabla \dot{d}\}, \quad \mathcal{F} = \{\mathbf{P}, \mathbf{T}, Y, f, \boldsymbol{\xi}\}. \quad (2.5)$$

The internal power expenditure per unit volume takes the form

$$\mathcal{P}_{\text{int}} = \mathbf{P} : \dot{\mathbf{F}} + \mathbf{T} : \dot{\mathbf{F}}^p + Y \dot{\bar{\varepsilon}}^p + f \dot{d} + \boldsymbol{\xi} \cdot \nabla \dot{d}, \quad (2.6)$$

and the external power expenditure is assumed to be zero, i.e. no surface traction, body force, or the so-called micro-forces, $\mathcal{P}_{\text{ext}}(\mathcal{V}) = 0$.

Let ψ be the Helmholtz free energy per unit volume in the reference configuration. Assuming no external volumetric heat source, the total entropy rate, the internal entropy production rate and the external entropy input rate per unit volume can be rearranged as

$$\rho T \dot{s} = \rho T \dot{s}_{\text{int}} + \rho T \dot{s}_{\text{ext}}, \quad (2.7a)$$

$$\rho T \dot{s}_{\text{int}} \equiv \mathcal{P}_{\text{int}} - \dot{\psi} - \frac{1}{T} \mathbf{q} \cdot \nabla T \geq 0, , \quad (2.7b)$$

$$\rho T \dot{s}_{\text{ext}} \equiv -\nabla \cdot \mathbf{q} + \frac{1}{T} \mathbf{q} \cdot \nabla T, \quad (2.7c)$$

where ρ is the reference density, and \mathbf{q} is the heat flux. Substituting (2.6) into (2.7b) yields the local dissipation inequality

$$\rho T \dot{s}_{\text{int}} = \mathbf{P} : \dot{\mathbf{F}} + \mathbf{T} : \dot{\mathbf{F}}^p + Y \dot{\bar{\varepsilon}}^p + f \dot{d} + \boldsymbol{\xi} \cdot \nabla \dot{d} - \dot{\psi} - \frac{1}{T} \mathbf{q} \cdot \nabla T \geq 0. \quad (2.8)$$

We assume that the generalized forces \mathbf{P} , \mathbf{T} and $\boldsymbol{\xi}$ are purely energetic, the generalized force Y is purely dissipative, and the generalized force f can be additively decomposed into an energetic part and a dissipative part. That is

$$\mathbf{P} = \mathbf{P}^{\text{en}}(\Lambda), \quad \mathbf{T} = \mathbf{T}^{\text{en}}(\Lambda), \quad Y = Y^{\text{dis}}(\dot{\bar{\varepsilon}}^p; \Lambda), \quad f = f^{\text{en}}(\Lambda) + f^{\text{dis}}(\dot{d}; \Lambda), \quad \boldsymbol{\xi} = \boldsymbol{\xi}^{\text{en}}(\Lambda). \quad (2.9)$$

The energetic forces depend only on the current thermodynamic state, while the dissipative forces depend only on the conjugate rate variables. Apparently, the dissipative forces must vanish in the quasi-static setting, i.e. $\lim_{\dot{\bar{\varepsilon}}^p \rightarrow 0^+} Y^{\text{dis}} = 0$ and $\lim_{\dot{d} \rightarrow 0^+} f^{\text{dis}} = 0$.

Let $a_{,b}$ denote the partial derivative of a with respect to b . The time derivative of the free energy density can be written as

$$\dot{\psi} = \psi_{,\mathbf{F}} : \dot{\mathbf{F}} + \psi_{,\mathbf{F}^p} : \dot{\mathbf{F}}^p + \psi_{,\varepsilon^c} \dot{\bar{\varepsilon}}^p + \psi_{,d} \dot{d} + \psi_{,\nabla d} \cdot \nabla \dot{d}. \quad (2.10)$$

Substituting (2.9) and (2.10) into (2.8) and applying the Coleman-Noll procedure lead to restrictions on the constitutive relations:

$$\boldsymbol{P} = \psi_{,\boldsymbol{F}}, \quad \boldsymbol{T} = \psi_{,\boldsymbol{F}^c}, \quad \psi_{,\varepsilon^c} = 0, \quad f^{\text{en}} = \psi_{,d}, \quad \boldsymbol{\xi} = \psi_{,\nabla d}, \quad (2.11)$$

and the dissipation inequality (2.8) reduces to

$$\rho T \dot{s}_{\text{int}} = Y \dot{\bar{\varepsilon}}^p + f^{\text{dis}} \dot{d} - \frac{1}{T} \boldsymbol{q} \cdot \nabla T \geq 0. \quad (2.12)$$

Substituting (2.12) and (2.7c) into (2.7a), and using the definition of entropy $s = -\rho\psi_{,T}$ and heat capacity $c \equiv -\rho T\psi_{,TT}$, the heat equation can be written as

$$\rho T \dot{s} = \rho c \dot{T} = -\nabla \cdot \boldsymbol{q} + Y \dot{\bar{\varepsilon}}^p + f^{\text{dis}} \dot{d}. \quad (2.13)$$

2.3 The minimization problem

2.4 Discretization

3

Brittle Fracture: Fracture in Microstructures

3.1 Introduction

3.2 Theory

3.2.1 *Constitutive choices*

3.2.2 *Approximation of the pressure boundary condition*

3.3 Verification

3.3.1 *Uniaxial traction of a bar*

3.3.2 *Pressurized crack propagation*

3.4 Numerical examples

3.4.1 *Effects of pore geometry, porosity, and loading conditions*

3.4.2 *High burnup structure fragmentation*

4

Cohesive Fracture: Soil Dessiontation

4.1 Introduction

In this work, a phase-field for cohesive fracture model is used to simulate pervasive cracking in thin films. A new elastic energy split is proposed to enforce frictionless contact conditions in the vicinity of diffuse fracture surfaces. In contrast to existing splits that have been proposed, our approach completely prevents tractions from being transmitted across fully damaged surfaces that are loaded in tension. Spatial variations of material properties are incorporated into our model, and we demonstrate, through forward analysis and by solving an inverse problem, how crack network morphology can be influenced by stochastic spatially-varying material properties.

The variational approach to fracture was proposed by Francfort and Marigo [2], and the phase-field implementation is attributed to Bourdin et al. [3]. Bourdin et al. [4] provides an overview. In the variational approach, crack surfaces are represented by a surface density function in terms of an auxiliary phase-field. This naturally gives rise to a regularization involving a length scale parameter. Such an approach is

known to be thermodynamically consistent and recent works have illustrated its potential to be predictive for a wide range of fracture problems. Phase-field for fracture models have succeeded in capturing complex crack patterns, including branching and coalescence in both two and three dimensions [5, 6, 7, 8, 9]. The approach has also been used to study the fracture of thin films, for example by Baldelli et al. [10, 11].

To prevent crack growth under compression, phase-field models of fracture typically employ some form of tension-compression asymmetric split in the elastic energy. Two popular approaches are the spectral decomposition [12, 13] and the volumetric-deviatoric decomposition [14]. Both the spectral decomposition and the volumetric-deviatoric decomposition are variational and lead to thermodynamically consistent fracture models. Although these variational approaches represent crack growth reasonably well for a broad range of problems, they do not completely preclude the transmission of tractions across fully damaged surfaces. In part, this is by design. The decompositions are designed to allow compressive tractions to be transmitted across fully damaged surfaces. But since they are developed from the full stress or strain as opposed to the surface tractions, they can also allow unwanted tensile or shear tractions to be transmitted. This can give rise to spurious macro-scale responses in some situations. Strobl and Seelig [15] proposed constitutive relations that satisfy the boundary conditions on diffuse crack surfaces by taking into account the crack orientation. Although the use of such a constitutive model violated the fundamental variational structure of phase-field models, it was shown to yield better results in some fracture problems [16]. A similar approach was presented by Fei and Choo [17, 18] to extend the model to better account for frictional contact conditions at crack surfaces. Finally, we mention the recent work of Lo et al. [19], in which the standard spectral split was modified to better guard against crack growth in compression.

In this work, we propose a variational elastic energy split that enforces frictionless

contact conditions. Importantly, the split effectively prevents the transmission of tractions across fully-damaged surfaces that are loaded in tension. The proposed split leads to a decomposition that is shown to be important in mode II and mixed-mode fracture problems. The new phase-field model is then applied to study the classical problem of the fracture of thin films bonded to thick substrates. Due to the accumulation of inelastic strain and the stiffness mismatch between the film and the substrate, cracks form either transversely through the thickness of the film, referred to as “channeling”, or at the interface, referred to as “debonding”. Film-substrate systems exist across a wide span of application problems, from technological systems such as nuclear fuel pellet–cladding interactions (PCI) [20, 21, 22, 23, 24] to more common civil infrastructure examples such as pavement asphalts [25, 26, 27, 28, 29]. The study of fracture in these systems is driven by an interest in both understanding the underlying mechanisms and in preventing crack nucleation and evolution. In the current work, we confine attention to transverse channeling cracks in the film. When a system of cracks nucleate, branch and coalesce, complicated crack networks appear in the thin films. Hutchinson and Suo [30] provides a comprehensive review of crack patterns in film-substrate systems.

The fracture of thin films bonded to substrates has been studied using model-based simulations based on a wide range of methodologies. These problems are challenging to simulate because they involve pervasive crack nucleation, branching, and coalescence. Phenomenological spring models were developed and employed by Crosby and Bradley [31], Leung and Néda [32] and Sadhukhan et al. [33]. Zhang et al. [34] applied a cohesive zone method to study the film-substrate interface debonding, and Sánchez et al. [35] proposed a mesh fragmentation technique to simulate three-dimensional crack morphologies. Although such techniques are known to produce mesh-dependent results, the resulting crack networks were found to be satisfactory. Liang et al. [36], Sukumar and Prévost [37] and Huang et al. [38] modeled thin film

cracking using the eXtended Finite Element Method (XFEM) which allowed for the cracks to evolve independently of the finite-element mesh.

The aforementioned analytical and numerical efforts have provided a great deal of insight into the factors controlling the fracture of thin films. In particular, the mechanical properties that govern the spacing between cracks have been studied by Hutchinson and Suo [30], Xia and Hutchinson [39] and most recently by Yin et al. [40]. In contrast, the connection between spatial variations in material properties and the morphology of the resulting crack patterns has received fairly little attention. This is despite experimental evidence that crack morphologies are sensitive to spatial variations in material properties, see, e.g. Kitsunezaki et al. [41, 42], Halász et al. [43], Kitsunezaki et al. [44] and Nakahara et al. [45]. To our knowledge, while some previous model-based simulations of thin-film fracture have incorporated random material properties, they have not specifically considered spatial fluctuations and the construction of proper stochastic models. More broadly, the literature on probabilistic modeling for fracture simulations remains scarce. In [46], variability in fracture strength was estimated from multiscale simulations, and spatially-varying mesoscale properties were subsequently integrated into an asynchronous spacetime discontinuous Galerkin finite element based fracture model to study the impact on fragmentation. The integration of apparent elasticity coefficients in a multiscale-informed phase-field formulation was investigated in [47], with the aim of reproducing variability in the macroscopic response. The fracture toughness was modeled as deterministic and homogeneous, and was identified by solving an inverse problem. In [48], a continuum mapping of the meso-scale structure to the packing fraction at the macro-scale was employed to introduce a random component to phase-field simulations of surfactant-induced fracture of particle rafts. In this work, we construct a probabilistic model for the critical fracture energy and the fracture toughness, modeled as (potentially correlated) random fields, and examine their influence on the

random morphology of the resulting fracture patterns.

Our model-based simulations of thin-film fracture for systems with spatially-variable material properties are facilitated in this work through the adoption of an extension of phase-field models to cohesive fracture [49, 50, 51]. Phase-field for cohesive fracture models incorporate the original proposition by Xia and Hutchinson [39] regarding a “critical fracture energy”. The regularization length is decoupled from the material properties in these approaches, and the critical strength and the fracture toughness of the material are no longer strongly correlated. This independence permits simulations of drying in systems with realistic material properties for typical clays or soils, for example, without compromising the magnitude of the critical strength or requiring regularization lengths that are larger than the specimen dimensions. It also allows systems with spatially-variable fracture properties to be studied using a spatially-constant regularization length, greatly improving the fidelity of the numerical calculations.

This paper is organized as follows. ?? provides the theoretical background for phase-field models of fracture, the new decomposition, associated solution algorithms, and stochastic models for fracture properties. In ??, several numerical examples of benchmark problems in quasi-static fracture mechanics are provided to illustrate the efficacy of the new approach to enforcing frictionless contact conditions. The main results of this work are provided in ??, where the new model is used to study the formation of crack networks in thin films and in soil dessication problems. In particular, model-based simulations are used to examine how the fragment statistics and fracture morphologies are influenced by spatial variations in the fracture properties. Comparisons with both theory and experimental observations are provided. Finally, a summary and some concluding remarks are provided in the last section.

4.2 Theory

4.2.1 Constitutive choices

To solve the energy minimization problem, we first find the necessary conditions for the minimizer of the objective function by temporarily relaxing the constraint, i.e. by solving the unconstrained version as:

$$\min_{\mathbf{u}, d} \tilde{\Psi}_{\text{total}} = -\tilde{\Psi}_{\text{external}} + \tilde{\Psi}_{\text{internal}} + \tilde{\Psi}_{\text{fracture}}. \quad (4.1)$$

The Euler-Lagrange equations for this unconstrained minimization problem state that the minimizer satisfies:

$$-\nabla \cdot \frac{\delta \Psi_{\text{total}}}{\delta \nabla \mathbf{u}} + \frac{\delta \Psi_{\text{total}}}{\delta \mathbf{u}} + \frac{d}{dt} \frac{\delta \Psi_{\text{total}}}{\delta \dot{\mathbf{u}}} = \mathbf{0}, \quad (4.2a)$$

$$-\nabla \cdot \frac{\delta \Psi_{\text{total}}}{\delta \nabla d} + \frac{\delta \Psi_{\text{total}}}{\delta d} + \frac{d}{dt} \frac{\delta \Psi_{\text{total}}}{\delta \dot{d}} = 0. \quad (4.2b)$$

For the quasi-static fracture problems (under the small strain assumption) studied in this work, the total energy can be written in terms of displacements \mathbf{u} and damage d as:

$$\begin{aligned} \Psi_{\text{total}} = & - \underbrace{\left(\int_{\partial\Omega} \boldsymbol{\tau} \cdot \mathbf{u} \, dA + \int_{\Omega} \mathbf{b} \cdot \mathbf{u} \, dV \right)}_{\text{external energy}} + \underbrace{\int_{\Omega} g(d) \psi_{\text{elastic}}^{(A)} \, dV + \int_{\Omega} \psi_{\text{elastic}}^{(I)} \, dV}_{\text{degraded elastic energy}} \\ & + \underbrace{\int_{\Omega} \frac{\mathcal{G}_c}{c_0 l} (w(d) + l^2 \|\nabla d\|^2) \, dV}_{\text{approx. fracture energy}}, \end{aligned} \quad (4.3)$$

where $\boldsymbol{\tau}$ is the surface traction and \mathbf{b} is the body force. Substituting the total energy into the Euler-Lagrange equations, we obtain the necessary conditions of the minimizer, which are essentially the governing equations of the given system together

with boundary conditions:

$$-\boldsymbol{\nabla} \cdot \tilde{\boldsymbol{\sigma}} - \mathbf{b} = \mathbf{0}, \quad \text{in } \Omega, \quad (4.4)$$

$$-\boldsymbol{\nabla} \cdot \boldsymbol{\xi} + Mw'(d) + g'(d)\psi_{\text{elastic}}^{\langle A \rangle} = 0, \quad \text{in } \Omega, \quad (4.5)$$

$$\tilde{\boldsymbol{\sigma}} \cdot \mathbf{n} = \boldsymbol{\tau}, \quad \text{on } \partial\Omega, \quad (4.6)$$

$$\boldsymbol{\xi} \cdot \mathbf{n} = 0, \quad \text{on } \partial\Omega, \quad (4.7)$$

with constitutive relations

$$\tilde{\boldsymbol{\sigma}} = g(d) \frac{\delta \psi_{\text{elastic}}^{\langle A \rangle}}{\delta \boldsymbol{\nabla} \mathbf{u}} + \frac{\delta \psi_{\text{elastic}}^{\langle I \rangle}}{\delta \boldsymbol{\nabla} \mathbf{u}}, \quad (4.8)$$

$$\boldsymbol{\xi} = M\kappa \boldsymbol{\nabla} d + g(d) \frac{\delta \psi_{\text{elastic}}^{\langle A \rangle}}{\delta \boldsymbol{\nabla} d} + \frac{\delta \psi_{\text{elastic}}^{\langle I \rangle}}{\delta \boldsymbol{\nabla} d}, \quad (4.9)$$

where $\tilde{\boldsymbol{\sigma}}$ is the degraded stress tensor, $\boldsymbol{\xi}$ is the thermodynamic conjugate to $\boldsymbol{\nabla} d$ (the dependence of $\psi_{\text{elastic}}^{\langle A \rangle}$ and $\psi_{\text{elastic}}^{\langle I \rangle}$ on $\boldsymbol{\nabla} d$ is defined in ??), $\kappa = 2l^2$ is the interfacial coefficient, and $M = \frac{g_c}{c_0 l}$ is often referred to the mobility in keeping with general Allen-Cahn phase-field models. According to (??), and due to the fact that $\boldsymbol{\xi}|_{d=0} = \mathbf{0}$, the damage begins to accumulate as soon as:

$$\psi_{\text{elastic}}^{\langle A \rangle} > \psi_c = -M \frac{w'(0)}{g'(0)}, \quad (4.10)$$

where ψ_c is a model-specific energy threshold for damage initiation. For example, a brittle fracture model that uses $w(d) = d^2$ results in a critical energy $\psi_c = 0$, and cohesive-type fracture models that use $w(d) = d$ have a critical energy $\psi_c = -M/g'(0)$. In this work, we adopt a cohesive fracture model that uses the local dissipation function $w(d) = d$ in conjunction with the degradation function proposed by Lorentz [52, 53] such that the critical fracture energy is not necessarily correlated with the other material properties and model parameters, i.e. the fracture toughness

\mathcal{G}_c and the length scale l :

$$g(d; p \geq 1) = \frac{(1-d)^2}{(1-d)^2 + \frac{M}{\psi_c} d(1+pd)}, \quad (4.11)$$

where p controls the size of the fracture process zone and is chosen to be 1 in this work.

4.2.2 Enforcing the traction-free boundary condition

For quasi-static mechanical-fracture coupling, the energy balance and thus the corresponding energy minimization problem can be instantiated as:

$$\begin{aligned} & \min_{u,d} \left(-\tilde{\Psi}_{\text{external}}|_{\Omega,\partial\Omega} + \tilde{\Psi}_{\text{internal}}|_{\Omega} + \tilde{\Psi}_{\text{fracture}}|_{\Omega} \right), \\ & \text{subject to } \dot{d} \geq 0. \end{aligned} \quad (4.12)$$

A typical assumption in fracture mechanics is that only tensile/expansive components of the elastic energy contribute to crack initiation and growth. Therefore, the degraded elastic energy is often split into an active part that is coupled with fracture, and an inactive part that is independent of fracture. According to the split of elastic energy, we have:

$$\tilde{\Psi}_{\text{elastic}} = \int_{\Omega} g(d) \psi_{\text{elastic}}^{\langle A \rangle} \, dV + \int_{\Omega} \psi_{\text{elastic}}^{\langle I \rangle} \, dV. \quad (4.13)$$

Widely used active/inactive splits are spectral split [12, 13] and volumetric-deviatoric split [9]. Unfortunately, neither the spectral split nor the volumetric-deviatoric split completely prevent tensile or shear tractions from being transmitted across fully-damaged surfaces. Accordingly, we now develop a split that is motivated by the consideration of frictionless contact conditions along fully damaged surfaces.

We begin by recalling the standard Kuhn-Tucker optimality conditions for frictionless contact under small deformation, which can be written as

$$t_N \geq 0, \quad u_I \leq 0, \quad t_N u_I = 0, \quad (4.14)$$

where t_N is the contact pressure and u_I denotes the interpenetration between the contact surfaces. The contact pressure is typically obtained from the stress and the unit outward normal to the contact surface. In regularized models of fracture, however, it can be difficult to identify a unique surface based on the damage field. Accordingly, we rely on the gradient of the damage field to construct an approximate normal $\tilde{\mathbf{n}}$, viz.

$$\tilde{\mathbf{n}} = \frac{\nabla d}{\|\nabla d\|}, \quad (4.15)$$

and calculate the normal pressure as

$$t_N = -\tilde{\mathbf{n}} \cdot \boldsymbol{\sigma} \cdot \tilde{\mathbf{n}}. \quad (4.16)$$

Our split keys off the sign of the normal pressure, by isolating the cases of a positive pressure (for contact) from a negative pressure (for opening). In particular, we construct a “normal-tangential” stress decomposition of the form

$$\boldsymbol{\sigma} = \boldsymbol{\sigma}_n^+ + \boldsymbol{\sigma}_n^- + \boldsymbol{\sigma}_t, \quad (4.17)$$

where

$$\boldsymbol{\sigma}_n^\pm = \langle -t_N \rangle_\pm \tilde{\mathbf{n}} \otimes \tilde{\mathbf{n}}, \quad \boldsymbol{\sigma}_t = \boldsymbol{\sigma} - \boldsymbol{\sigma}_n^+ - \boldsymbol{\sigma}_n^-, \quad (4.18)$$

with $\langle -t_N \rangle_\pm := (-t_N \pm |-t_N|)/2$ denoting a signed version of the standard Macaulay bracket.

In the vicinity of the regularized crack surface, we then propose the use of a stress-based elastic energy split, hereafter referred to as the *contact split*, that takes

the form:

$$\psi_{\text{elastic}} = \psi_{\text{elastic}}^{\langle A \rangle} + \psi_{\text{elastic}}^{\langle I \rangle}, \quad (4.19\text{a})$$

$$\psi_{\text{elastic}}^{\langle A \rangle} = \frac{1}{2} \boldsymbol{\sigma}^{\langle A \rangle} : \boldsymbol{\varepsilon}, \quad \psi_{\text{elastic}}^{\langle I \rangle} = \frac{1}{2} \boldsymbol{\sigma}^{\langle I \rangle} : \boldsymbol{\varepsilon}, \quad (4.19\text{b})$$

$$\boldsymbol{\sigma}^{\langle A \rangle} = \boldsymbol{\sigma}_n^+ + \boldsymbol{\sigma}_t, \quad \boldsymbol{\sigma}^{\langle I \rangle} = \boldsymbol{\sigma}_n^-. \quad (4.19\text{c})$$

The corresponding constitutive relation follows as:

$$\tilde{\boldsymbol{\sigma}} = \frac{\delta \tilde{\psi}_{\text{elastic}}}{\delta \boldsymbol{\varepsilon}} = g(d) \frac{\delta \psi_{\text{elastic}}^{\langle A \rangle}}{\delta \boldsymbol{\varepsilon}} + \frac{\delta \psi_{\text{elastic}}^{\langle I \rangle}}{\delta \boldsymbol{\varepsilon}}, \quad (4.20\text{a})$$

$$= g(d) \frac{\delta}{\delta \boldsymbol{\varepsilon}} \left(\frac{1}{2} \boldsymbol{\sigma}^{\langle A \rangle} : \boldsymbol{\varepsilon} \right) + \frac{\delta}{\delta \boldsymbol{\varepsilon}} \left(\frac{1}{2} \boldsymbol{\sigma}^{\langle I \rangle} : \boldsymbol{\varepsilon} \right), \quad (4.20\text{b})$$

$$= g(d) \boldsymbol{\sigma}^{\langle A \rangle} + \boldsymbol{\sigma}^{\langle I \rangle}, \quad (4.20\text{c})$$

and

$$\boldsymbol{\xi} = M\kappa \boldsymbol{\nabla} d + g(d) \frac{\delta \psi_{\text{elastic}}^{\langle A \rangle}}{\delta \boldsymbol{\nabla} d} + \frac{\delta \psi_{\text{elastic}}^{\langle I \rangle}}{\delta \boldsymbol{\nabla} d}, \quad (4.21)$$

where

$$\frac{\delta \psi_{\text{elastic}}^{\langle A \rangle}}{\delta \boldsymbol{\nabla} d} = - \frac{\delta \psi_{\text{elastic}}^{\langle I \rangle}}{\delta \boldsymbol{\nabla} d} = \frac{1}{\|\boldsymbol{\nabla} d\|} [2 \langle -t_N \rangle_- \varepsilon_N \tilde{\boldsymbol{n}} - H(t_N) \varepsilon_N \boldsymbol{\sigma} \cdot \tilde{\boldsymbol{n}} - \langle -t_N \rangle_- \boldsymbol{\varepsilon} \cdot \tilde{\boldsymbol{n}}],$$

$$(4.22)$$

and H denotes the Heaviside function.

It bears emphasis that the proposed elastic energy split only serves to enforce the crack surface traction free boundary condition, and it is not reasonable to expect it to reliably govern crack nucleation and growth. In the present work, to ensure that such a normal-tangential split is applied only in the vicinity of the crack surface, we impose a simple threshold d_{critical} such that we apply

$$\begin{cases} \text{the contact split (4.19a) to (4.20c), } d \geq d_{\text{critical}} \\ \text{the strain-based spectral split [12, 13], } d < d_{\text{critical}}. \end{cases}$$

Remark. Alternative to a threshold, in principle a total energy could be constructed using a blending function that transitions between a standard split and the contact split.

It can be shown that the definition of the contact pressure (4.16) follows by relaxing the frictionless constraint into a minimization problem, and t_N is therefore the best scalar quantity one can choose to approximate the traction-free boundary condition:

$$\min_{t_N} \|\boldsymbol{\sigma}_t(t_N) \cdot \tilde{\mathbf{n}}\|^2 \quad (4.23a)$$

$$= \|(\boldsymbol{\sigma} - \langle -t_N \rangle_+ \tilde{\mathbf{n}} \otimes \tilde{\mathbf{n}} - \langle -t_N \rangle_- \tilde{\mathbf{n}} \otimes \tilde{\mathbf{n}}) \cdot \tilde{\mathbf{n}}\|^2 \quad (4.23b)$$

$$= \|(\boldsymbol{\sigma} + t_N \tilde{\mathbf{n}} \otimes \tilde{\mathbf{n}}) \cdot \tilde{\mathbf{n}}\|^2 \quad (4.23c)$$

$$= t_N^2 + 2t_N \tilde{\mathbf{n}} \cdot \boldsymbol{\sigma} \cdot \tilde{\mathbf{n}} + \|\boldsymbol{\sigma} \cdot \tilde{\mathbf{n}}\|^2, \quad (4.23d)$$

and the minimizer is

$$t_N = \arg \min_{t_N} (t_N^2 + 2t_N \tilde{\mathbf{n}} \cdot \boldsymbol{\sigma} \cdot \tilde{\mathbf{n}} + \|\boldsymbol{\sigma} \cdot \tilde{\mathbf{n}}\|^2) = -\tilde{\mathbf{n}} \cdot \boldsymbol{\sigma} \cdot \tilde{\mathbf{n}}. \quad (4.24)$$

4.2.3 Stochastic models for fracture properties

In the current work, we allow for material property inhomogeneity in the macroscopic continuum model. Specifically, we introduce the random field $\{\boldsymbol{P}(\mathbf{x}) = (P_1(\mathbf{x}), P_2(\mathbf{x})), \mathbf{x} \in \Omega\}$ defined on the probability space (Θ, Σ, P) , indexed by Ω and with values in $\mathbb{R}_{>0} \times \mathbb{R}_{>0}$, such that $\{P_1(\mathbf{x}), \mathbf{x} \in \Omega\}$ (respectively $\{P_2(\mathbf{x}), \mathbf{x} \in \Omega\}$) is a prior representation of $\{\mathcal{G}_c(\mathbf{x}), \mathbf{x} \in \Omega\}$ (respectively $\{\psi_c(\mathbf{x}), \mathbf{x} \in \Omega\}$). Due to the restrictions on the state space, the bivariate random field $\{\boldsymbol{P}(\mathbf{x}), \mathbf{x} \in \Omega\}$ is non-Gaussian. In order to model nongaussianity, the random field $\{\boldsymbol{P}(\mathbf{x}), \mathbf{x} \in \Omega\}$ is *defined* as

$$\boldsymbol{P}(\mathbf{x}) := \mathcal{T}(\boldsymbol{\Xi}(\mathbf{x}), \mathbf{x}), \quad \forall \mathbf{x} \in \Omega, \quad (4.25)$$

where \mathcal{T} is a measurable, nonlinear mapping and $\{\boldsymbol{\Xi}(\mathbf{x}), \mathbf{x} \in \Omega\}$ is a centered Gaussian random field with values in \mathbb{R}^2 to be defined momentarily. From a method-

ological standpoint, it should be noticed that the transformation \mathcal{T} is constructed *a priori* and used to define $\{\mathbf{P}(\mathbf{x}), \mathbf{x} \in \Omega\}$ such that the latter constitutes a surrogate capturing some essential features of $\{(\mathcal{G}_c(\mathbf{x}), \psi_c(\mathbf{x})), \mathbf{x} \in \Omega\}$ (while exhibiting a low dimensional parameterization). In general, the existence of a nonlinear mapping \mathcal{T} such that (4.25) holds for a *given* non-Gaussian field is not guaranteed; see, e.g., [54].

Construction of the Non-Gaussian Model

In this work, the transformation \mathcal{T} is constructed by imposing the family $\{f_{\mathbf{x}}\}_{\mathbf{x} \in \Omega}$ of first-order marginal distributions:

$$P_{\mathbf{P}(\mathbf{x})}(d\mathbf{p}) = f_{\mathbf{x}}(\mathbf{p})d\mathbf{p}, \quad \forall \mathbf{x} \in \Omega, \quad (4.26)$$

where $f_{\mathbf{x}}$ is the probability density function of $\mathbf{P}(\mathbf{x})$, \mathbf{x} being fixed in Ω , and $d\mathbf{p} = dp_1dp_2$ is the Lebesgue measure in \mathbb{R}^2 . It is assumed that $f_{\mathbf{x}}(\cdot) = f(\cdot; \mathbf{w}_{\mathbf{x}})$, where $\mathbf{w}_{\mathbf{x}}$ is a vector-valued hyperparameter indexed by $\mathbf{x} \in \Omega$. In order to simplify the analysis, we assume from now on that the aforementioned hyperparameter does not depend on location, and we write $f_{\mathbf{x}}(\cdot) = f(\cdot; \mathbf{w})$ using a slight abuse of notation.

The construction of f can be achieved in many different ways. In what follows, the construction is performed by assuming that (i) \mathcal{G}_c and ψ_c (together with their inverses) are positive and have finite variance, for physical consistency, and (ii) the two fracture properties can exhibit some level of correlation. In accordance with information theory [55, 56] and more precisely, with the principle of maximum entropy [57, 58], the first assumption leads to the consideration of Gamma marginal distributions. Following the notation introduced above, we shall impose that

$$P_{P_1(\mathbf{x})}(dp_1) = f_{\mathcal{G}}(p_1; (\underline{p}_1, \delta_1))dp_1, \quad \forall \mathbf{x} \in \Omega, \quad (4.27)$$

and

$$P_{P_2(\mathbf{x})}(dp_2) = f_{\mathcal{G}}(p_2; (\underline{p}_2, \delta_2))dp_2, \quad \forall \mathbf{x} \in \Omega, \quad (4.28)$$

where $f_{\mathcal{G}}(\cdot; (\underline{p}, \delta))$ denotes the univariate Gamma probability density function with mean \underline{p} and coefficient of variation δ . In this setting, the joint distribution of $\mathbf{P}(\mathbf{x})$ must be constructed from the knowledge of the marginal laws associated with $P_1(\mathbf{x})$ and $P_2(\mathbf{x})$. This ill-posed problem does not admit a unique solution, and many possible forms were proposed in the case of a bivariate Gamma distribution (see, e.g., Chapter 8 in [59] for a review). Here, we use the bivariate Gamma distribution derived by Moran using a copula [60]:

$$f(\mathbf{p}) = \frac{1}{\sqrt{1-\rho^2}} \exp \left\{ -\frac{1}{2(1-\rho^2)} [(\rho \tilde{p}_1)^2 - 2\rho \tilde{p}_1 \tilde{p}_2 + (\rho \tilde{p}_2)^2] \right\} f_{\mathcal{G}}(p_1; (\underline{p}_1, \delta_1)) f_{\mathcal{G}}(p_2; (\underline{p}_2, \delta_2)), \quad (4.29)$$

where $\rho \in (-1, 1)$ is the (Pearson) correlation coefficient between $P_1(\mathbf{x})$ and $P_2(\mathbf{x})$ (\mathbf{x} being fixed), and

$$\tilde{p}_i = \Phi^{-1}(F_{\mathcal{G}}(p_i; (\underline{p}_i, \delta_i))) , \quad i \in \{1, 2\} , \quad (4.30)$$

where Φ^{-1} is the inverse of the univariate Gaussian distribution function and $F_{\mathcal{G}}(\cdot; (\underline{p}_i, \delta_i))$ is the univariate Gamma distribution function with mean \underline{p}_i and coefficient of variation δ_i (which is associated with $f_{\mathcal{G}}(\cdot; (\underline{p}_i, \delta_i))$), and that the extreme cases $\rho = \pm 1$ are also well defined; see [60]. Notice that the vector of hyperparameters then reads as $\mathbf{w} = (\underline{p}_1, \delta_1, \underline{p}_2, \delta_2, \rho)$. It follows that

$$P_1(\mathbf{x}) = F_{\mathcal{G}}^{-1}(\Phi(\Upsilon_1(\mathbf{x})); (\underline{p}_1, \delta_1)) \quad (4.31)$$

and

$$P_2(\mathbf{x}) = F_{\mathcal{G}}^{-1}(\Phi(\Upsilon_2(\mathbf{x})); (\underline{p}_2, \delta_2)) \quad (4.32)$$

for any \mathbf{x} fixed in Ω , where $\Upsilon(\mathbf{x}) = (\Upsilon_1(\mathbf{x}), \Upsilon_2(\mathbf{x}))$ is a centered Gaussian random

variable with covariance matrix [60]:

$$[C_{\Upsilon}] = \begin{bmatrix} 1 & \rho \\ \rho & 1 \end{bmatrix}. \quad (4.33)$$

Upon using the Cholesky factorization $[C_{\Upsilon}] = [L_{\Upsilon}]^T [L_{\Upsilon}]$, it can be deduced that $\{\mathbf{P}(\mathbf{x}), \mathbf{x} \in \Omega\}$ can be defined through

$$P_1(\mathbf{x}) = F_{\mathcal{G}}^{-1}(\Phi(\Xi_1(\mathbf{x})); (\underline{p}_1, \delta_1)), \quad \forall \mathbf{x} \in \Omega, \quad (4.34)$$

and

$$P_2(\mathbf{x}) = F_{\mathcal{G}}^{-1}(\Phi(\rho \Xi_1(\mathbf{x}) + \sqrt{1 - \rho^2} \Xi_2(\mathbf{x})); (\underline{p}_2, \delta_2)), \quad \forall \mathbf{x} \in \Omega, \quad (4.35)$$

where $\{\Xi(\mathbf{x}) = (\Xi_1(\mathbf{x}), \Xi_2(\mathbf{x})), \mathbf{x} \in \mathbb{R}^n\}$ is a centered Gaussian random field with statistically independent, centered Gaussian components such that $\Upsilon(\mathbf{x}) = [L_{\Upsilon}]^T \Xi(\mathbf{x})$, $\forall \mathbf{x} \in \Omega$. Equations (4.34) and (4.35) define the nonlinear mapping \mathcal{T} introduced in Equation (4.25) such that $\mathbf{P}(\mathbf{x}) = \mathcal{T}(\Xi(\mathbf{x}))$, for all $\mathbf{x} \in \Omega$ (note that the spatial dependence of the transformation was dropped given the retained modeling assumptions). This relation can equivalently be stated as $\mathbf{P}(\mathbf{x}) = \mathcal{T}^*(\Upsilon(\mathbf{x}))$, with obvious notation. The Gaussian random fields are defined in the next section.

Construction of the Underlying Gaussian Models

In accordance with the periodic assumption retained in the mechanical modeling framework, it is assumed that each random field $\{\Xi_i(\mathbf{x}), \mathbf{x} \in \mathbb{R}^n\}$, $i \in \{1, 2\}$, satisfies the invariance property $\Xi_i(\mathbf{x}) = \Xi_i(\mathbf{x} + p\mathbf{x}')$ for all $\mathbf{x} \in \Omega$ and $\mathbf{x}' \in \mathbb{Z}^n$ P -almost surely, where it is assumed (without loss of generality) that $\Omega = ([0, p])^n$. Consequently, the centered random field $\{\Xi(\mathbf{x}), \mathbf{x} \in \mathbb{R}^n\}$ is uniquely defined by its restriction to Ω . Assuming the stationary of this restriction in Ω , the underlying Gaussian field is defined through the matrix-valued covariance function

$\boldsymbol{\tau} \mapsto [R_{\Xi}(\boldsymbol{\tau})] = \mathbb{E}\{\Xi(\mathbf{x} + \boldsymbol{\tau}) \otimes \Xi(\mathbf{x})\}$ such that

$$[R_{\Xi}(\boldsymbol{\tau})] = \begin{bmatrix} R_1(\boldsymbol{\tau}) & 0 \\ 0 & R_2(\boldsymbol{\tau}) \end{bmatrix}, \quad \forall \boldsymbol{\tau} \in ([0, p])^n, \quad (4.36)$$

where R_1 and R_2 are the p -periodic covariance functions defining (the restrictions of) $\{\Xi_1(\mathbf{x}), \mathbf{x} \in \mathbb{R}^n\}$ and $\{\Xi_2(\mathbf{x}), \mathbf{x} \in \mathbb{R}^n\}$ (to Ω), respectively. For the sake of illustration, we assume similar covariance functions for the two Gaussian components, setting $R_1 = R_2 = R$, and we consider the case of a separable covariance function in \mathbb{R}^2 :

$$R(\boldsymbol{\tau}) = R_1(\tau_1) \times R_2(\tau_2). \quad (4.37)$$

We further assume that R_1 and R_2 only differ in the choice of hyperparameters, so that the above equation can be written, using an abuse of notation, as

$$R(\boldsymbol{\tau}) = R(\tau_1; L_1) \times R(\tau_2; L_2), \quad (4.38)$$

where $L_1 > 0$ and $L_2 > 0$ are model parameters controlling the correlation ranges of the fields along the directions defined by the canonical basis in \mathbb{R}^2 . The univariate covariance function R is assumed to take the generic form

$$R_\phi(\tau; L) = \exp(-c\phi(\tau; L)), \quad \forall \tau \in [0, p], \quad (4.39)$$

where c is a positive constant (that depends on both ϕ and L) to be defined and ϕ is a p -periodic function taken as

$$\phi(\tau; L) = \frac{|\sin(\pi\tau/p)|}{L} \quad (\text{Periodic Exponential, PE}), \quad (4.40)$$

or

$$\phi(\tau; L) = \frac{\sin^2(\pi\tau/p)}{L^2} \quad (\text{Periodic Squared-Exponential, PSE}). \quad (4.41)$$

The subscript in the notation R_ϕ underlines the choice of a particular periodic function. The two functions defined by (4.40) and (4.41) are specifically chosen so as to investigate the impact of sample path regularity on fracture simulation outcomes. In particular, and while both functions yield random fields of fracture properties that are mean-square continuous, the periodic squared-exponential covariance function obtained by combining (4.39) and (4.41) leads to mean-square differentiable fields which exhibit “smooth” realizations. On the contrary, the periodic exponential function defined by considering (4.40) yields random fields that are not mean-square differentiable and thus have much rougher realizations.

In order to ensure meaningful comparison between the covariance models, the normalization constants are determined such that the spatial correlation length along the direction of one main direction is equal to L , that is:

$$\int_0^{p/2} |R_\phi(\tau; L)| d\tau = L . \quad (4.42)$$

For later use, we introduce the normalized correlation length $L^* = L/p$. For the squared exponential model, the constant c_{PSE} is hence required to satisfy the non-linear equation

$$\frac{1}{2} p \exp\left(-\frac{c_{\text{PSE}}}{2L^2}\right) I_0\left(\frac{c_{\text{PSE}}}{2L^2}\right) = L , \quad (4.43)$$

where I_0 is the 0th order modified Bessel’s function, whereas the constant c_{PE} associated with the exponential covariance kernel must satisfy

$$\frac{1}{2} p \left[I_0\left(\frac{c_{\text{PE}}}{L}\right) - S_0\left(\frac{c_{\text{PE}}}{L}\right) \right] = L , \quad (4.44)$$

where S_0 is the 0th order modified Struve’s function. In this work, these equations are solved numerically using a Newton-Raphson solver.

It should be noticed that the covariance function $\boldsymbol{\tau} \mapsto [\mathbf{R}_{\mathbf{T}}(\boldsymbol{\tau})]$ defining the restriction of the Gaussian random field $\{\mathbf{T}(\mathbf{x}), \mathbf{x} \in \mathbb{R}^n\}$ to Ω is given by

$$[\mathbf{R}_{\mathbf{T}}(\boldsymbol{\tau})] = \begin{bmatrix} \mathbf{R}_1(\boldsymbol{\tau}) & \rho \mathbf{R}_1(\boldsymbol{\tau}) \\ \rho \mathbf{R}_1(\boldsymbol{\tau}) & \rho^2 \mathbf{R}_1(\boldsymbol{\tau}) + (1 - \rho^2) \mathbf{R}_2(\boldsymbol{\tau}) \end{bmatrix}, \quad \forall \boldsymbol{\tau} \in ([0, p])^n, \quad (4.45)$$

which shows the role played by the parameter ρ on the covariance function of $\{P_2(\mathbf{x}), \mathbf{x} \in \Omega\}$ (after the action of \mathcal{T}^*).

Fundamental Properties of the Random Field of Fracture Properties

Based on the construction proposed in Sections ?? and ??, the non-Gaussian random field $\{\mathbf{P}(\mathbf{x}), \mathbf{x} \in \Omega\}$ modeling the fracture properties satisfies the following properties:

1. $P_i(\mathbf{x}) > 0$ for all $\mathbf{x} \in \Omega$ and $i \in \{1, 2\}$, almost surely.
2. $\{\mathbf{P}(\mathbf{x}), \mathbf{x} \in \Omega\}$ is of second order, $\mathbb{E}\{|0\mathbf{P}(\mathbf{x})|0^2\} < +\infty \quad \forall \mathbf{x} \in \Omega$.
3. The field satisfies $\mathbf{P}((0, x_2)) = \mathbf{P}((p, x_2))$ and $\mathbf{P}((x_1, 0)) = \mathbf{P}((x_1, p))$, almost surely.
4. The mean function $\mathbf{x} \mapsto \underline{\mathbf{p}}(\mathbf{x}) = \mathbb{E}\{\mathbf{P}(\mathbf{x})\}$ is given by $\underline{\mathbf{p}}(\mathbf{x}) = \underline{\mathbf{p}} = (\underline{p}_1, \underline{p}_2)$ for all $\mathbf{x} \in \Omega$.
5. The covariance matrix at any location $\mathbf{x} \in \Omega$ reads as

$$\mathbb{E}\{(\mathbf{P}(\mathbf{x}) - \underline{\mathbf{p}}) \otimes (\mathbf{P}(\mathbf{x}) - \underline{\mathbf{p}})\} = \begin{bmatrix} \underline{p}_1^2 \delta_1^2 & \underline{p}_1 \underline{p}_2 \delta_1 \delta_2 \rho \\ \underline{p}_1 \underline{p}_2 \delta_1 \delta_2 \rho & \underline{p}_2^2 \delta_2^2 \end{bmatrix}. \quad (4.46)$$

It can also be deduced that the random field $\{\mathbf{P}(\mathbf{x}), \mathbf{x} \in \Omega\}$ is mean-square continuous for the PE and PSE correlation functions introduced in Section ???. Finally, the field is mean-square differentiable for the PSE covariance function.

Recall that in the properties above, \underline{p}_1 and \underline{p}_2 correspond to the desired mean values for the fracture toughness \mathcal{G}_c and energy threshold ψ_c , and δ_1 and δ_2 are the coefficients of variation that control the statistical dispersions of these parameters. The parameter ρ measures the level of correlation between the fracture properties.

Stochastic Simulation Aspects

Simulating realizations of the random field of fracture properties requires (i) drawing realizations of the underlying Gaussian random fields defined in ??, and (ii) evaluating the nonlinear transformations defined by (4.34) and (4.35). Routines to compute the latter mappings are readily available in many scientific computing environments. Regarding the generation of the Gaussian fields, we presently resort to truncated Karhunen-Loève expansions. Each (mean-square continuous) random field $\{\Xi_i(\mathbf{x}), \mathbf{x} \in \mathbb{R}^n\}$, $i \in \{1, 2\}$, is thus expanded as

$$\Xi_i(\mathbf{x}) = \sum_{k=1}^{q_i} \sqrt{\lambda_k} \eta_k \varphi_k(\mathbf{x}) , \quad (4.47)$$

where $\{\eta_k\}_{k \geq 1}$ is a set of independent normalized Gaussian random variables, and $\{\lambda_k\}_{k \geq 1}$ and $\{\varphi_k\}_{k \geq 1}$ are the nonnegative eigenvalues (ordered as a nonincreasing sequence) and the associated orthonormal eigenfunctions of the covariance function that satisfy the following integral equation (which is a Fredholm integral equation of the second kind):

$$\int_{\Omega} R(\mathbf{x}, \mathbf{x}') \varphi_k(\mathbf{x}') d\mathbf{X}' = \lambda_k \varphi_k(\mathbf{x}) , \quad \forall \mathbf{x} \in \Omega , \quad (4.48)$$

where R is the covariance kernel introduced in Section ?? (note the abuse of notation, with $\boldsymbol{\tau} = \mathbf{x} - \mathbf{x}'$). For arbitrary covariance functions, this integral equation can be solved by using a standard Galerkin formulation [61, 62]: given a finite set of basis

functions $\{\phi_j\}_{j=1}^{N_{\text{node}}} \subset L_2(\Omega)$, each eigenfunction is approximated as

$$\varphi_k(\mathbf{x}) \approx \sum_{j=1}^{N_{\text{node}}} \alpha_j^{(k)} \phi_j(\mathbf{x}) . \quad (4.49)$$

Substituting this approximation in the integral equation and enforcing the residual to be orthogonal to $\text{span}(\{\phi_j\}_{j=1}^{N_{\text{node}}})$, we obtain

$$\sum_{j=1}^{N_{\text{node}}} \alpha_j^{(k)} \int_{\Omega} \int_{\Omega} R(\mathbf{x}, \mathbf{x}') \phi_j(\mathbf{x}') \phi_\ell(\mathbf{x}) \, d\mathbf{X}' \, d\mathbf{X} = \sum_{j=1}^{N_{\text{node}}} \alpha_j^{(k)} \int_{\Omega} \lambda_j \phi_j(\mathbf{x}) \phi_\ell(\mathbf{x}) \, d\mathbf{X} . \quad (4.50)$$

Considering the above equation for all eigenfunctions leads to the generalized eigenvalue problem $[K][A] = [\Lambda][M][A]$, where $[A]_{j\ell} = \alpha_j^{(\ell)}$, $[\Lambda]_{j\ell} = \lambda_j \delta_{j\ell}$ (with $\delta_{j\ell}$ the Kronecker delta), and $[K]$ and $[M]$ are the matrices with entries

$$[K]_{j\ell} = \int_{\Omega} \int_{\Omega} R(\mathbf{x}, \mathbf{x}') \phi_j(\mathbf{x}') \phi_\ell(\mathbf{x}) \, d\mathbf{X}' \, d\mathbf{X} , \quad [M]_{j\ell} = \int_{\Omega} \phi_j(\mathbf{x}) \phi_\ell(\mathbf{x}) \, d\mathbf{X} . \quad (4.51)$$

For each Gaussian field $\{\Xi_i(\mathbf{x}), \mathbf{x} \in \mathbb{R}^n\}$, the truncation order $q_i \leq N_{\text{node}}$ can be determined by analyzing the convergence of the error function

$$\varepsilon_{\text{KL}}(q) = 1 - \left(\sum_{k=1}^q \lambda_k \sqrt{\sum_{k=1}^{N_{\text{node}}} \lambda_k} \right) , \quad (4.52)$$

and by selecting q_i such that $\varepsilon_{\text{KL}}(q_i) \leq \varepsilon_0$ for some given tolerance $0 < \varepsilon_0 \ll 1$.

4.3 Verification

4.3.1 Mode I: Edge-Notched Unilateral Tension Test

Consider a $1 \text{ mm} \times 1 \text{ mm}$ plate with a pre-existing crack on the left side, loaded in uniaxial tension, as shown in Figure 4.1a. We assume the plate to be composed of an

isotropic material with Young’s modulus $E = 2.1 \times 10^5$ MPa, Poisson’s ratio $\nu = 0.3$, fracture toughness $\mathcal{G}_c = 2.7$ mJ mm $^{-2}$, and critical strength $\sigma_c = 2.5 \times 10^3$ MPa. The plate is fixed along the bottom, and the top surface is displaced in the vertical direction. Roller supports are also assumed to be in place, such that the horizontal displacement vanishes along the top surface. The plate is assumed to be sufficiently thick such that plane strain conditions hold.

The domain is meshed with linear triangular elements. The maximum/minimum element characteristic lengths are 0.05 mm and 0.005 mm, respectively, corresponding to a mesh with 7845 elements. The crack surface density is approximated with a regularization length $l = 0.015$ mm, such that the half phase-field bandwidth is resolved by approximately 6 elements.

We examine two representations of the pre-existing crack. First, we use a “geometric notch” to represent the crack as shown in Figures 4.1b and 4.2a. In this case, the traction-free boundary condition on the notch surfaces is satisfied in a weak sense. The resulting damage fields as a function of boundary displacement are shown in Figures 4.2b to 4.2d. Only the damage fields obtained using the spectral decomposition are shown in the Figures. Contours of the damage field obtained using the contact split with a threshold were found to be indistinguishable.

Secondly, we use an initial damage field $d(t = 0) = d_0$ to represent the initial crack, where d_0 is given by:

$$d_0(\mathbf{x}) = \begin{cases} \left(1 - \frac{\tau(\mathbf{x})}{2l}\right)^2, & \tau(\mathbf{x}) \leq 2l \\ 0, & \tau(\mathbf{x}) > 2l \end{cases} \quad (4.53)$$

$$\text{with} \quad (4.54)$$

$$\tau(\mathbf{x}) = \begin{cases} |\mathbf{x} \cdot \mathbf{e}_2|, & \mathbf{x} \cdot \mathbf{e}_1 \leq 0, \\ \|\mathbf{x}\|, & \mathbf{x} \cdot \mathbf{e}_1 > 0, \end{cases} \quad (4.55)$$

with an origin for the coordinate system at the center of the plate. The initial damage

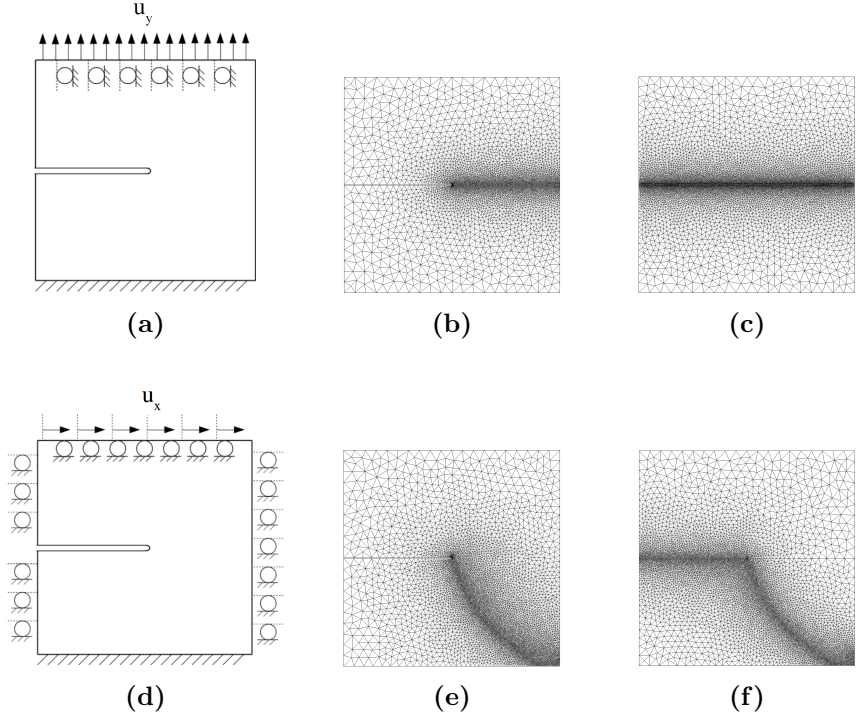


FIGURE 4.1. Boundary conditions of the plate with a pre-existing crack for (a) a mode I tension test and (d) a mode II shear test. Finite element meshes for the mode I calculations (b - c) and for the mode II calculations (e - f). For (b, e) the meshes have the initial crack geometry “meshed-in” while (c, f) have local refinement around the initial damage field. All meshes are pre-refined along the predicted crack-path with a characteristic element size of 0.005 mm.

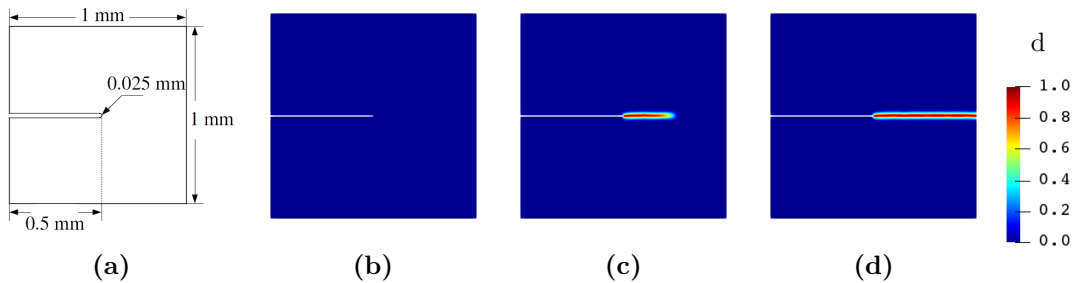


FIGURE 4.2. Edge-notched specimen loaded in tension with initial crack represented by a geometric notch with a rounded corner. (a) Dimensions of the notched plate. Damage d at (b) $u_y = 0$ mm, (c) $u_y = 0.0048$ mm, (d) $u_y = 0.006$ mm.

field is resolved using the locally refined mesh of linear triangular elements shown in Figure 4.1c. The resulting initial damage field is shown in Figure 4.3b. Once again,

the contour plots of the damage field obtained using a spectral decomposition and the contact split were found to be indistinguishable.

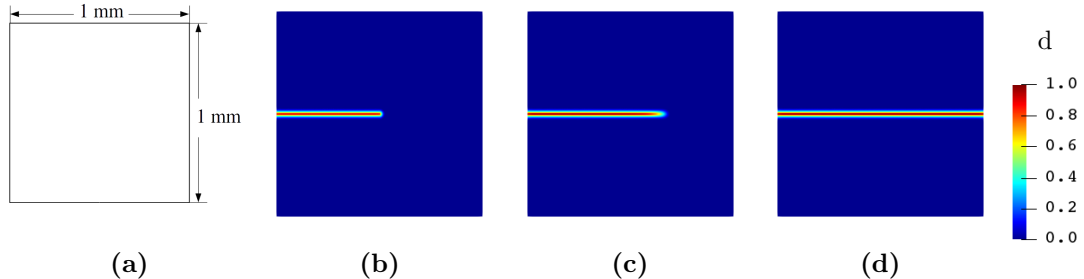


FIGURE 4.3. Edge-notched specimen loaded in tension with initial crack represented by a damage field. (a) Dimensions of the intact plate. The Damage d at (b) $u_y = 0 \text{ mm}$ (c) $u_y = 0.0048 \text{ mm}$ (d) $u_y = 0.006 \text{ mm}$.

Plots of the vertical component of the reaction force at the top boundary of the plate versus the prescribed y -displacement are shown in Figure 4.4, for both representations of the initial crack and split strategies. The reaction force is nondimensionalized with respect to the critical strength and the plate thickness, i.e. $f_y^* = f_y / (\sigma_c t)$, and the displacement is nondimensionalized by $u_y^* = u_y / a$, where a is the side length of the square plate. As expected, the contact split does not affect the material response in the uniaxial loading case (Figure 4.4a), and the results appear to be relatively insensitive to the choice of threshold for switching between the spectral split and the contact split (Figure 4.4b).

4.3.2 Mode II: Edge-Notched Shear Test

The effect of the proposed energy split becomes readily apparent when the loading case is dominated by in-plane or out-of-plane shear. Let us consider the same edge-notched thick plate as in the last section, but subjected to a different loading. A schematic of the boundary conditions for this case and the corresponding meshes are shown in Figures 4.1d to 4.1f.

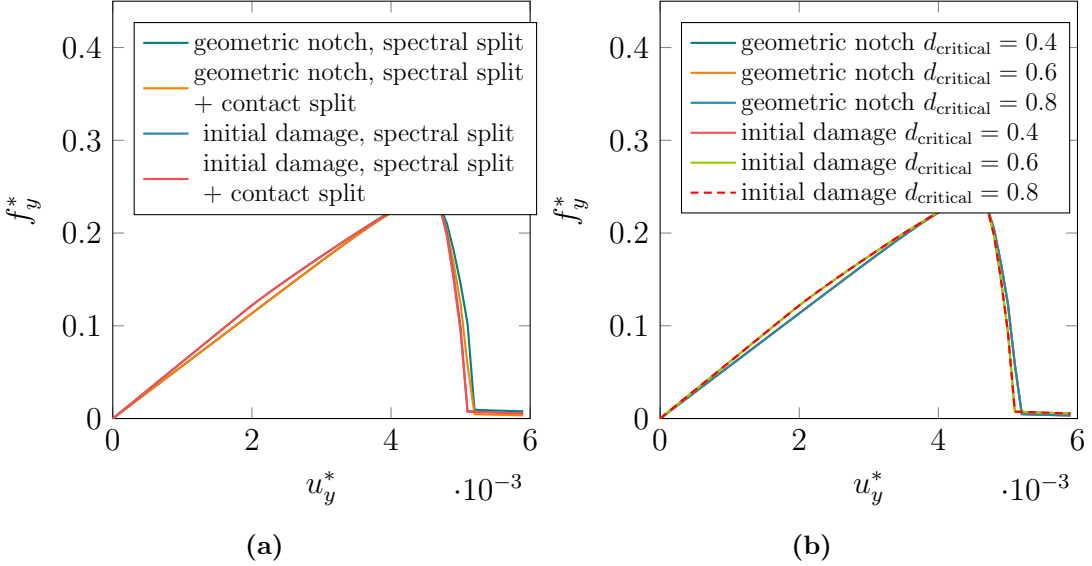


FIGURE 4.4. Mode I force–displacement curves obtained using (a) the spectral decomposition with two representations of the pre-existing crack (b) a spectral decomposition in conjunction with the contact split with different critical damage threshold on two representations of the pre-existing crack.

Once again, the effect of the contact split is examined by comparing the results using two different representations of the initial crack, as shown in Figure 4.5 and Figure 4.6a. Simulations that rely solely on the spectral decomposition result in dramatically different crack paths (Figures 4.5c, 4.5d, 4.5g and 4.5h) and force-displacement responses (Figure 4.6a). We note that after the initial decay following a horizontal displacement of $u_x = 1.0 \times 10^{-2} \text{ mm}$, the force for the geometric notch with the spectral decomposition begins to rise. Even though the damage field completely separates the plate into two sections, the force continues to increase. This is because the spectral decomposition does not prevent all traction from being transmitted across a fully damaged surface.

In contrast, when the traction-free condition is enforced using the contact split, the crack paths (Figures 4.5c, 4.5d, 4.5k and 4.5l) as well as the force-displacement curves (Figure 4.6b) are similar for both representations of the pre-existing crack. Notably in this case, the force at the boundary decays completely to zero as the plate

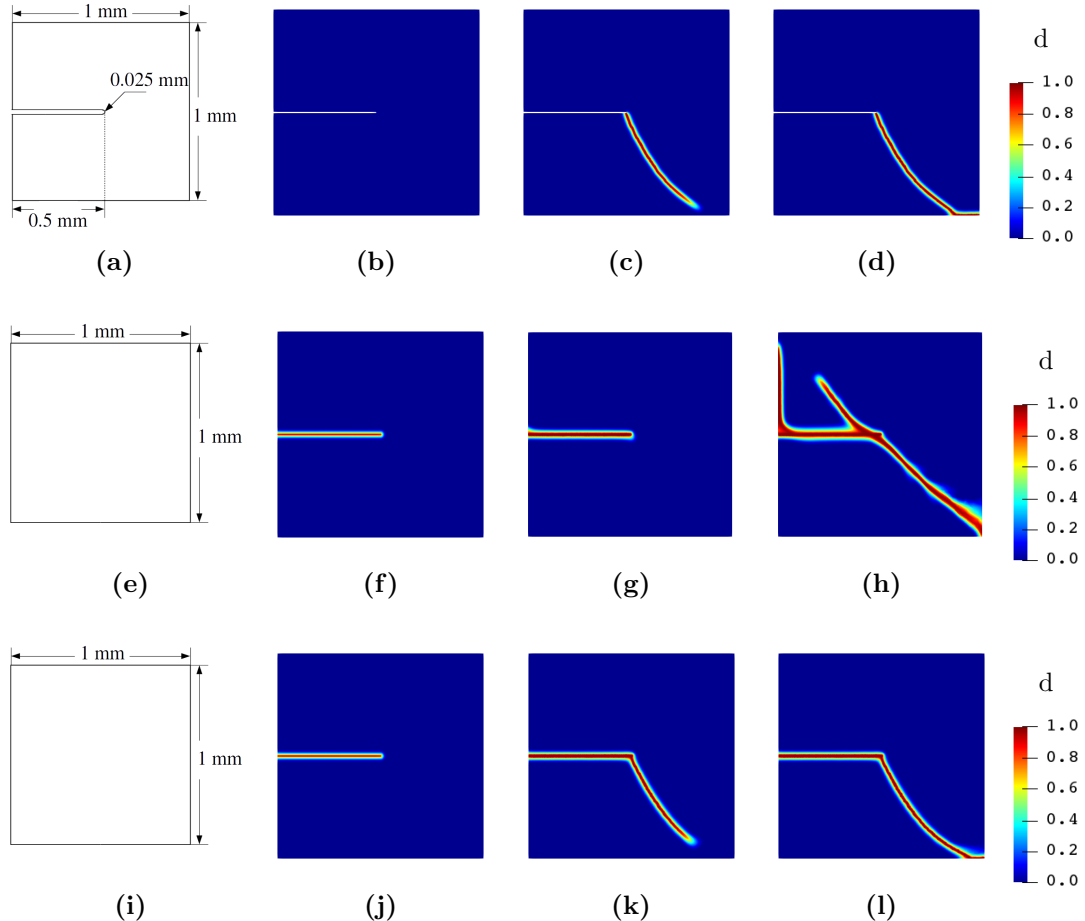


FIGURE 4.5. The crack paths obtained using (a-d) the spectral decomposition on a geometrically notched plate, (e-h) the spectral decomposition with an initial damage field d_0 (4.53) representing the initial crack, and (i-l) the contact split with an initial damage field. Snapshots of crack paths are shown at (b,f,j) $u_x = 0$ mm, (c,g,k) $u_x = 0.0109$ mm, and (d,h,l) $u_x = 0.02$ mm.

is separated in two by the damage field. As shown in Figure 4.6b, the results are also relatively insensitive to the particular choice of threshold for the contact split.

We note that if the threshold is selected to be too high (e.g. $d_{\text{critical}} \geq 0.8$) a small upward perturbation in the force-displacement curve can be observed, shortly after a horizontal displacement of $u_x = 1.0 \times 10^{-2}$ mm. The brief increase is due to the fact that the band of damage wherein the contact split is applied is too small, and some traction can still be transmitted across the fully damaged band. Essentially, there are

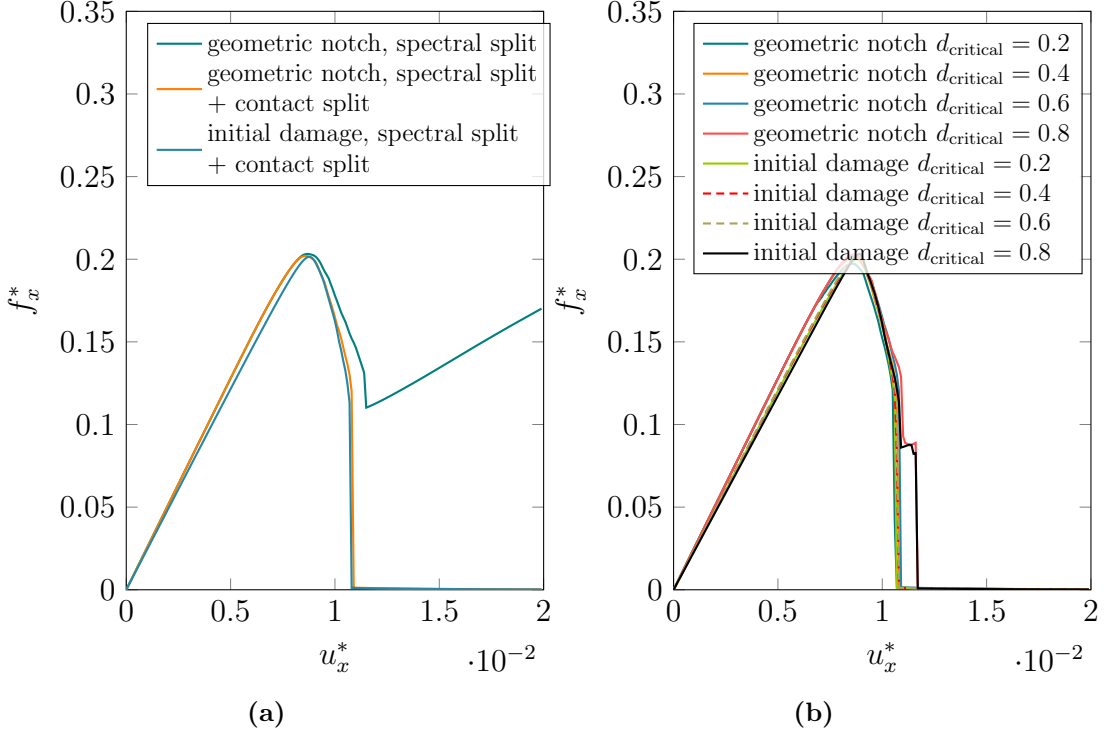


FIGURE 4.6. Mode II force–displacement curves obtained using (a) spectral decomposition with two representations of the initial crack (b) spectral decomposition in conjunction with the contact split with different critical damage threshold on two representations of the initial crack.

elements capturing the peak damage field wherein some quadrature points are below the threshold while others are above it. While further mesh refinement can remove this artifact, in practice we employ meshes that sufficiently capture the phase-field regularization, wherein $2l/h^e = 5$. Given this level of mesh refinement and typical damage profiles, we anticipate that a threshold of $d_{\text{critical}} = 0.6$ is sufficient to prevent any such artifacts. As such, we employ a threshold of $d_{\text{critical}} = 0.6$ for all subsequent problems.

4.3.3 Crack Propagation Under Biaxial Tension

We now examine a problem in which a thin plate with initial imperfections is subject to biaxial tension. Plane-stress conditions are assumed to hold. The plate geometry

and boundary conditions are summarized in Figure 4.7a, and the initial damage field representing two imperfections is shown in Figure 4.7b. Periodic boundary conditions are assumed on all sides.

Using property values that are representative of a typical clay specimen, the plate is assumed to be composed of a material with a Young's modulus E of 4 MPa, a Poisson's ratio ν of 0.2, a fracture toughness \mathcal{G}_c of 27 kJ m^{-2} , and a critical fracture energy ψ_c of 30 J m^{-2} .

The governing equation for the mechanical problem in this case is given by:

$$\nabla \cdot (\tilde{\boldsymbol{\sigma}} + \sigma_0 \mathbf{I}) = 0, \quad (4.56)$$

where σ_0 is a scalar-valued function that varies temporally and serves to model the drying process. The initial stress $\sigma_0 \mathbf{I}$ is equivalent to an inelastic eigen-strain, i.e. $\boldsymbol{\varepsilon}_0 = \mathbb{S} : (\sigma_0 \mathbf{I})$, where \mathbb{S} is the compliance tensor.

With a view towards nondimensionalization, as will be discussed in ??, the fracture driving force may be nondimensionalized as

$$\mathcal{D}^* = \sqrt{\frac{(1 - \nu^2)a}{E\mathcal{G}_c}} \sigma_0, \quad (4.57)$$

where a is a characteristic size for the domain. Here, we choose it to be the width of the plate.

We now compare simulation results obtained using three elastic energy split techniques: a no-split approach, the spectral split, and the contact split. The damage fields obtained using the three different split techniques are shown in Figure 4.8 at representative magnitudes of the dimensionless driving force.

The no-split approach treats the entire elastic energy as an active potential to be degraded, neglecting the tension-compression asymmetry. It is widely used in calculations of drying processes because the effective loading condition is assumed

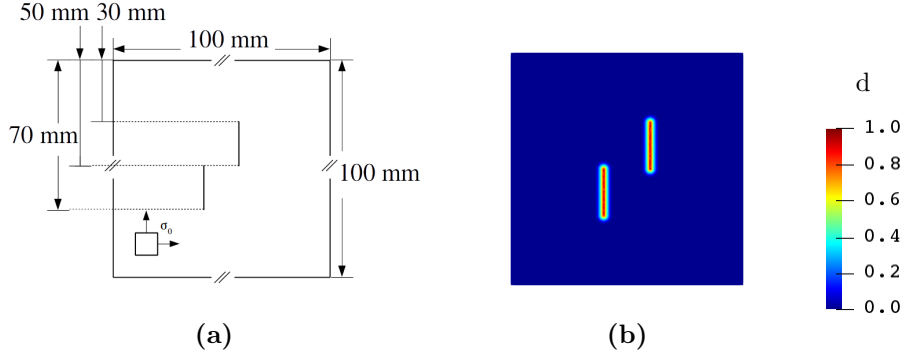


FIGURE 4.7. (a) Dimensions and boundary conditions of a thin plate with two parallel initial cracks. (b) The initial cracks are represented by an initial damage field.

to be tensile: biaxial tension in 2D and triaxial tension in 3D. However, we note that tensile loading conditions do not necessarily lead to a tensile local stress/strain state everywhere in the domain, hence it is possible to have crack propagation under compression, as can be observed in this example. We will return to this issue after examining the results obtained using a spectral decomposition and a spectral decomposition with the contact split.

The spectral decomposition prevents crack propagation under compression (Figure 4.8d), but without enforcing the traction-free condition on the crack surfaces represented by the damage field, which may affect secondary crack paths that emerge from existing crack surfaces (Figure 4.8e). Such artifacts can be removed by enforcing the traction-free condition on the regularized crack surfaces using the contact split (Figures 4.8g to 4.8i).

We now return to the issue of the possibility of crack growth under compression with a no-split approach. Comparing the damage profiles shown in Figures 4.8a, 4.8d and 4.8g one can observe that a damage bridge forms between the two vertical initial cracks only for the case of a no-split method. To explore this region more precisely, we consider the fields immediately before the bridge forms, and examine

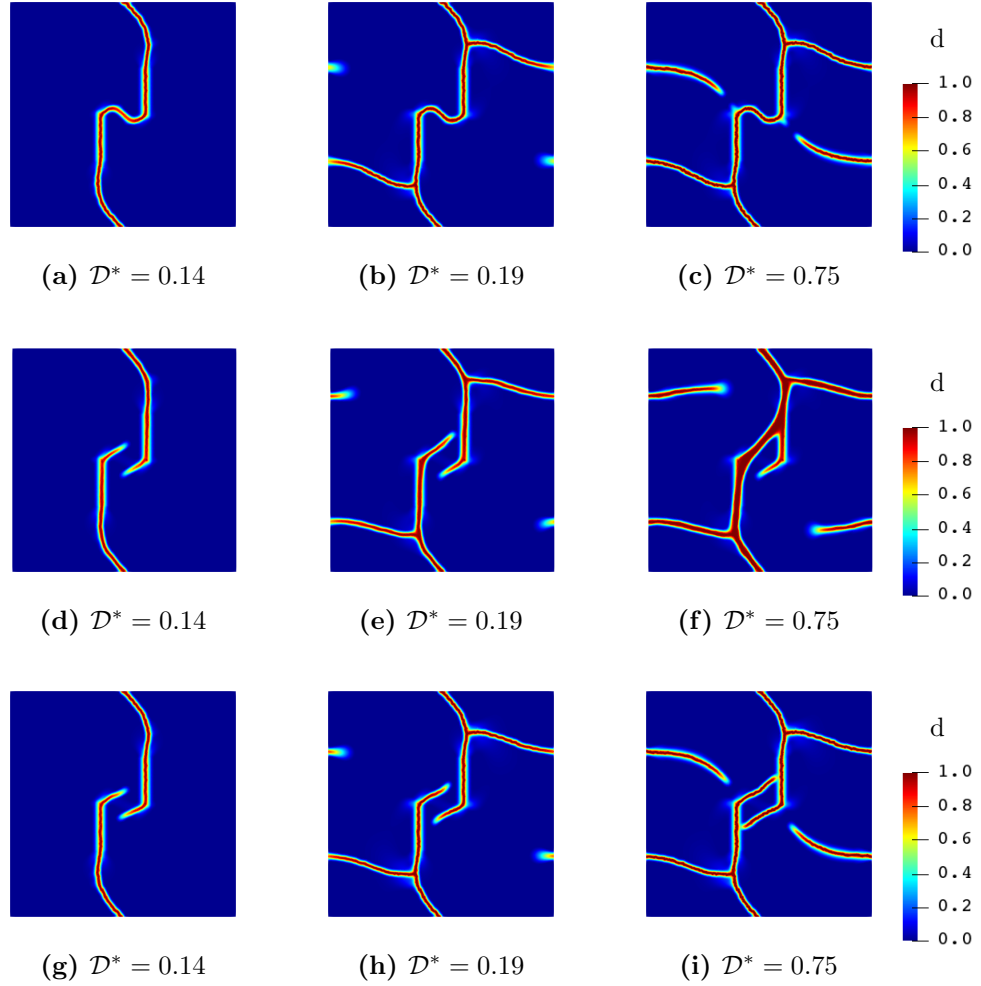


FIGURE 4.8. Crack paths obtained using (a-c) a no-split technique (d-f) the spectral decomposition (g-i) the contact split.

contour plots of the normal pressure for an orientation that is orthogonal to the bridge (Figure 4.9). The contour plots clearly indicate that the region is loaded in compression immediately before the bridge forms.

As a final observation in this section, we note that the crack-paths obtained using the spectral decomposition exhibit a broadening of the damage field at late stages of growth (Figure 4.8f). By contrast, the contact decomposition results in damage profiles that remain relatively thin compared to the specimen dimensions (Figure 4.8i).

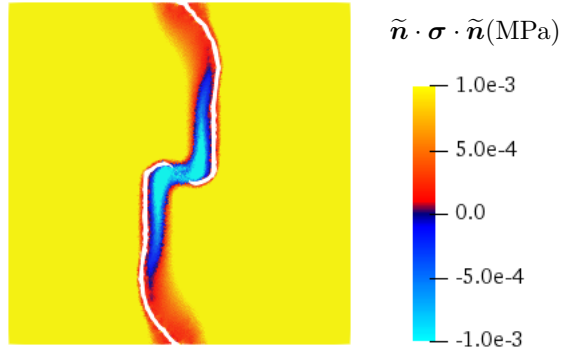


FIGURE 4.9. Contour plot of the normal pressure right before the bridge forms. The pressure is calculated for an orientation that is estimated to be orthogonal to the bridge. Elements within the contour of $d = 0.75$ are removed to indicate the current crack set.

4.3.4 Reconstruction of the marginal PDF

4.4 Numerical examples

In this section, we study in detail the formation of crack networks in thin films and soil dessication. We begin in Section ?? with a deterministic benchmark problem under quasi-one-dimensional conditions. The spacing between fractures is calculated as a function of the driving force with the cohesive fracture model and compared against a linear elasticity solution. Attention is then turned to an investigation of the stochastic aspects of fracture with a two-dimensional plane stress model in Section ??, wherein the fracture toughness and critical fracture energy are modeled as random fields. Finally, in Section ?? we present stochastic simulations of a soil dessication process in three dimensions.

4.4.1 One-Dimensional Simplification: Side View

We begin by deriving an analytical solution for the fracture of a thin film bonded to a thick substrate, as shown in Figure 4.10. Assuming that the planar dimensions of the film are much larger than its thickness, we first simplify the problem into a

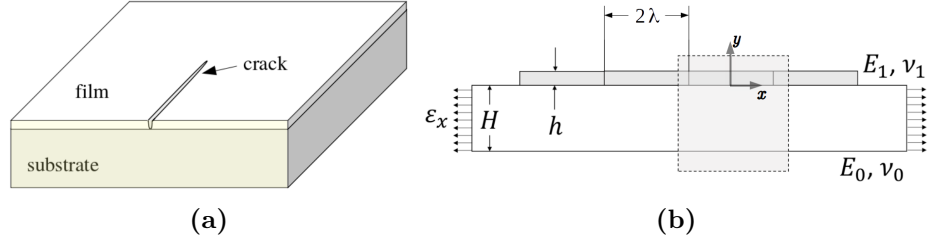


FIGURE 4.10. Description of a one-dimensional model for thin-film cracking. (a) Side view (highlighted in yellow) of the geometry (b) schematic representation of the side view. The elasticity solution is derived for the region highlighted with the shaded box, i.e. between the two discontinuities across the thin film. The coordinate system is centered at the middle of the bottom surface of the thin film.

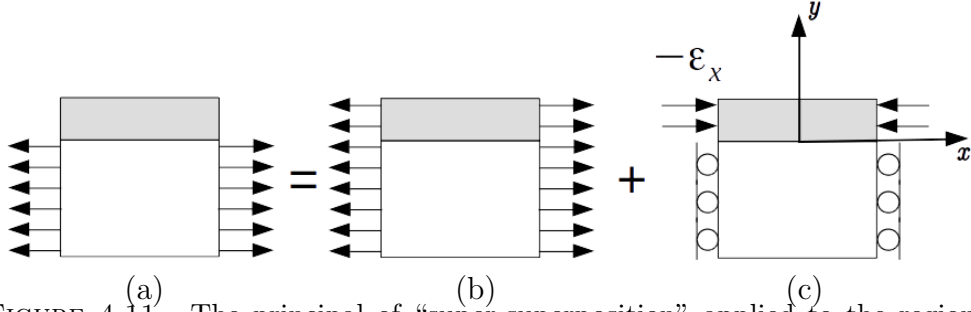


FIGURE 4.11. The principle of “super-superposition” applied to the region of interest marked in Figure 4.10b. The analytical solution is derived based on the boundary conditions shown in (c).

two-dimensional (or quasi 1D) plane-strain problem. The film is assumed to have Young’s modulus E_1 , Poisson’s ratio ν_1 , and thickness h . The substrate has Young’s modulus E_0 , Poisson’s ratio ν_0 , and thickness H . The fracture of the film is driven by the underlying substrate being stretched an amount ε_x . The problem with these simplifications and assumptions has been studied by many researchers, and analytical solutions from elasticity theory have been derived in several different ways. The derivation presented herein most closely follows that provided in Yin et al. [40].

With the increase of the tensile strain in the substrate, some uniformly distributed discontinuities with spacing 2λ form across the thickness of the film. We assume that no debonding occurs and that the vertical component of the displacement does not

vary in the horizontal direction, i.e.

$$u_y(x, y) = u_y(y). \quad (4.58)$$

The plane-strain equilibrium equation in the x-direction is written as

$$\frac{E_1}{1 - \nu_1^2} u_{x,xx} + \mu_1 u_{x,yy} = 0, \quad (4.59)$$

where μ_1 denotes the shear modulus of the film. This is supplemented by appropriate boundary conditions (Figure 4.11)

$$u_x(0, y) = 0, \quad (4.60)$$

$$u_{x,y}(x, h) = 0, \quad (4.61)$$

$$\frac{1}{h} \int_0^h \sigma_x(\lambda, y) dy = -\frac{E_1}{1 - \nu_1^2} \varepsilon_x. \quad (4.62)$$

We obtain the closed-form solution to the displacement field

$$u_x(x, y) = \varepsilon_x x - \frac{\sinh(cx/h)}{\cosh(c\lambda/h)} \frac{\cos(d(1 - y/h))}{\sin(d)} \sqrt{\frac{E_1}{\mu_1(1 - \nu_1^2)}} h \varepsilon_x, \quad (4.63)$$

where c and d are functions of Dundur's parameters α and β . Following [63, 39, 40], c and d can be computed as:

$$c = \frac{2}{\pi k(\alpha, \beta)}, \quad d = \sqrt{\frac{2}{1 - \nu_1}} c, \quad (4.64)$$

$$\alpha = \frac{\bar{E}_1 - \bar{E}_0}{\bar{E}_1 + \bar{E}_0}, \quad \beta = \frac{\mu_1(1 - 2\nu_0) - \mu_0(1 - 2\nu_1)}{2\mu_1(1 - \nu_0) + 2\mu_0(1 - \nu_1)}, \quad (4.65)$$

$$k(\alpha, \beta) \approx k(\alpha) = \frac{1.258 - 0.4\alpha - 0.26\alpha^3 - 0.3\alpha^4}{1 - \alpha}, \quad (4.66)$$

with $\bar{E}_0 = \frac{E_0}{(1 - \nu_0^2)}$, and $\bar{E}_1 = \frac{E_1}{(1 - \nu_1^2)}$. By replacing λ with $\lambda/2$, the crack opening

displacement can be written as

$$\delta(0, y) = 2 \tanh\left(\frac{c\lambda}{2h}\right) \frac{\cos(d(1 - y/h))}{\sin(d)} \sqrt{\frac{E_1}{\mu_1(1 - \nu_1^2)}} h \varepsilon_x. \quad (4.67)$$

Then the fracture toughness can be obtained as the work done to close the crack, i.e.

$$\mathcal{G}_c \cdot 2h = \int_0^h \sigma_x(0, y) \delta(0, y) \, dy, \quad (4.68)$$

$$\mathcal{G}_c = \frac{(1 - \nu_1^2)\sigma_x^2 h}{E_1 c} \left[2 \tanh\left(\frac{c\lambda}{2h}\right) - \tanh(c\lambda/h) \right]. \quad (4.69)$$

The amount of energy released by opening a transverse crack is governed by two dimensionless parameters:

$$\mathcal{D}^* = \sqrt{\frac{(1 - \nu_1^2)h}{E_1 \mathcal{G}_c}} \sigma_x, \quad l^* = \frac{\lambda}{h}. \quad (4.70)$$

It is then convenient to interpret the parameter \mathcal{D}^* as the dimensionless fracture driving energy and l^* as the dimensionless crack spacing. (4.69) can be rendered dimensionless following (4.70), and the relation between the dimensionless fracture driving energy and the dimensionless crack spacing can be written as

$$\mathcal{D}^* \mathcal{C}(l^*; c) = 1, \quad \mathcal{C}(l^*; c) = \frac{1}{c} \left[2 \tanh\left(\frac{1}{2} cl^*\right) - \tanh(cl^*) \right]. \quad (4.71)$$

In Figure 4.12a, we set the Poisson's ratio of both the film and the substrate to be $\nu_0 = \nu_1 = 0.2$, and plot the dimensionless fracture driving energy versus the dimensionless crack spacing for different combinations of the mismatch in the Young's modulus between the film and the substrate.

Next, we performed a series of numerical simulations using the phase-field for cohesive fracture model following the setup described in Figure 4.10b. Specifically,

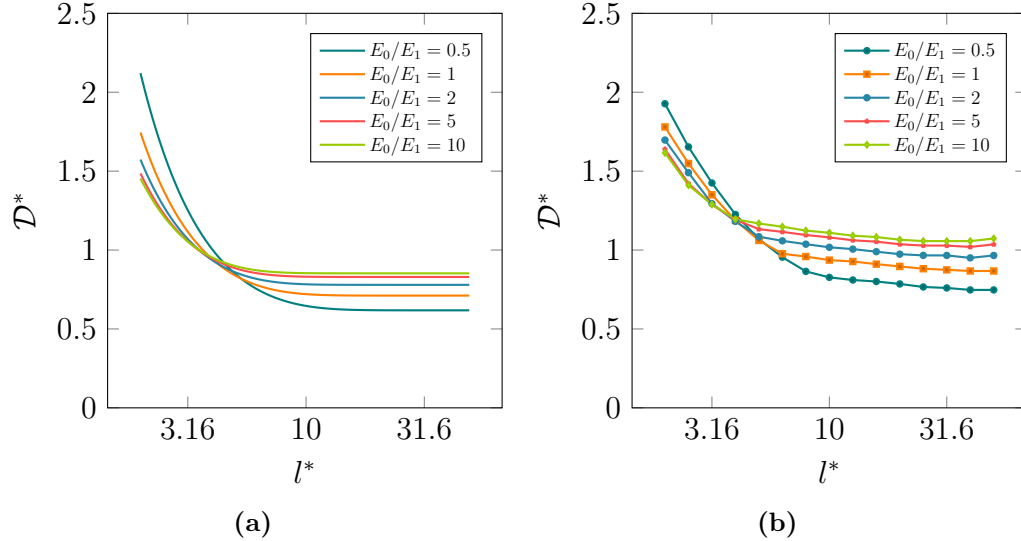


FIGURE 4.12. Relationship between the dimensionless fracture driving energy and the dimensionless crack spacing: (a) analytical solution using linear elasticity; and (b) numerically generated curves using the phase-field for cohesive model detailed in this work.

we examine the amount of driving energy required to propagate one transverse crack through the thickness of the film. The substrate and the film are represented by two rectangular domains $\Omega_0 = [-\lambda, \lambda] \times [-5 \text{ mm}, 0]$ and $\Omega_1 = [-\lambda, \lambda] \times [0, 1 \text{ mm}]$, respectively. The film-substrate system is the union of the two, i.e. $\Omega = \Omega_0 \cup \Omega_1$, and left-right periodicity is enforced. The substrate and the film are discretized with linear triangular elements with characteristic lengths of $h_0^e = \lambda/10$ and $h_1^e = \lambda/100$, respectively. The numerical results (Figure 4.12b) show a good agreement with the analytical solution.

4.4.2 Two-Dimensional Simplification: Stochastic Aspects of Fracture

We now consider a two-dimensional model of a thin film on a substrate wherein the geometry of the resulting fracture patterns is considerably more complex. For the bulk material properties, we adopt values that are representative of clay. The material properties and model parameters are summarized in Table 4.1.

We focus attention on the sensitivity of the resulting fracture patterns to stochastic spatial variations in the fracture properties. The random field of fracture properties $\{(\mathcal{G}_c(\mathbf{x}), \psi_c(\mathbf{x})), \mathbf{x} \in \Omega\}$ is defined and sampled following the model and procedures presented in ???. For all cases, the spatial correlation length L is larger than the regularization length l of the phase-field model. A tolerance of 1×10^{-3} is chosen for the truncation error in the Karhunen-Loëve expansion (4.52). The mean values of \mathcal{G}_c and ψ_c are chosen in accordance with reported values for clay as listed in Table 4.1. Coefficients of variation are chosen to be 0.03, leading to a variation of about $\pm 10\%$ around the mean value for the two random fracture parameters. All realizations shown in figures are normalized with respect to the corresponding stationary mean function, and the normalized quantities are denoted by \mathcal{G}_c^* and ψ_c^* .

Table 4.1. Summary of material properties and model parameters for all calculations in ??

Property/Parameter	Symbol	Value	Unit	Comment
Young's modulus	E	4	MPa	See [64, 1]
Poisson's ratio	ν	0.2	nondim.	See [64, 1]
Mean fracture toughness	$\underline{\mathcal{G}}_c$	27	kJ m^{-2}	See [65]
Mean critical fracture energy	$\underline{\psi}_c$	30	J m^{-2}	See [65]
Regularization length	l	0.5	mm	Such that $2l/h^e \approx 5$
Degradation shape parameter	p	1	nondim.	

A Plane-Stress Model

We now consider the problem of a thin film of thickness h that is bonded to an elastic underlayer of thickness H , as shown in Figure 4.13. The entire structure is assumed to be bonded to a rigid substrate. For this case, we employ the shear-lag model that is detailed in [36]. For the sake of clarity, the model is briefly described here.

We consider a square domain and assume the characteristic fragment sizes to be small compared to the overall specimen dimensions, and impose periodic boundary

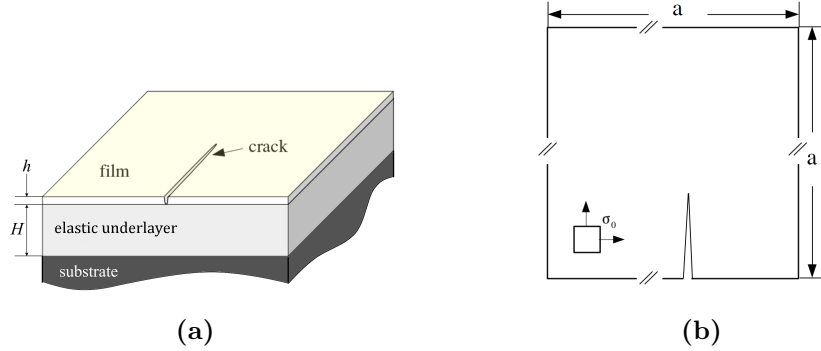


FIGURE 4.13. Description of a two-dimensional model for thin-film cracking. (a) Top view (highlighted in yellow) (b) schematic representation of the top view. A typical crack is shown to emphasize that fracture is only considered in the film.

conditions on all four boundaries. Assuming the underlying elastic layer is sufficiently thick and that the shear stress is uniform, equilibrium of a differential element of the film at the film-layer interface yields

$$\nabla \cdot \boldsymbol{\sigma} = \mu \frac{\mathbf{u}}{hH}, \quad (4.72)$$

where $\boldsymbol{\sigma} = \mathbb{C} : [\boldsymbol{\varepsilon} - \mathbb{S} : (\sigma_0 \mathbf{I})]$ is the stress, μ is the shear modulus of the elastic underlayer, and \mathbf{u} is the displacement. The corresponding potential energy representing the mismatch between the two sides of the film-layer interface can be written as

$$\psi_{\text{interface}} = \frac{1}{2} \frac{\mu}{hH} \|\mathbf{u}\|^2. \quad (4.73)$$

The underlying elastic layer is assumed to be much thicker than the film, i.e. $H = mh$, where $m \gg 1$. The interfacial energy can therefore be simplified as

$$\psi_{\text{interface}} = \frac{1}{2} \frac{\mu}{mh^2} \|\mathbf{u}\|^2. \quad (4.74)$$

The total energy of the simplified plane-stress model can then be written as

$$\begin{aligned} \Psi_{\text{total}} = & - \underbrace{\left(\int_{\partial\Omega} \boldsymbol{\tau} \cdot \mathbf{u} \, dA + \int_{\Omega} \mathbf{b} \cdot \mathbf{u} \, dV \right)}_{\text{external energy}} + \underbrace{\int_{\Omega} g(d) \psi_{\text{elastic}}^{(A)} \, dV + \int_{\Omega} \psi_{\text{elastic}}^{(I)} \, dV}_{\text{degraded elastic energy}} \\ & + \underbrace{\int_{\Omega} g(d) \frac{1}{2} \frac{\mu}{mh^2} \|\mathbf{u}\|^2 \, dV}_{\text{degraded interfacial energy}} + \underbrace{\int_{\Omega} \frac{3\mathcal{G}_c}{8l} (d + l^2 \|\nabla d\|^2) \, dV}_{\text{approx. fracture energy}} \end{aligned} \quad (4.75)$$

For all calculations in ??, we assume $\frac{\mu}{mh^2} = 0.1$.

The square domain is discretized using linear triangular elements with a characteristic length of $h^e = a/500$. This mesh is used for the displacement subproblem for linear elasticity, the phase-field subproblem for fracture, and the generalized eigenvalue problem for the random fields. The displacement field and the damage field are constrained to be a -periodic, and the random fields are constructed to be a -periodic as well.

Effect of Correlation Length and Smoothness

To study the effect of the correlation length, crack patterns for four different values of L are compared. Ten calculations, corresponding to ten samples of the stochastic fields, are carried out for each value of L . Representative random fields and their corresponding damage fields are shown in Figure 4.14. A Flooding algorithm (described in ??) is used to group elements into clusters in a volume-preserving way, to facilitate the counting of distinct fragments. Following the one-dimensional derivation (??), two dimensionless parameters are extracted as

$$\mathcal{D}^* = \sqrt{\frac{(1 - \nu_1^2)h}{E_1 \underline{\mathcal{G}_c}}} \sigma_0, \quad l^* = \frac{\lambda}{h}, \quad \lambda \approx \sqrt{A}, \quad (4.76)$$

where the crack spacing λ is estimated from the fragment area A . Dimensionless curves are plotted in Figure 4.16.

As expected, it is seen that the PSE covariance model generates smoother realizations. As the normalized correlation length $L^* = L/p$ becomes larger, i.e. Figures 4.14c, 4.14i and 4.14o, a substantial amount of damage accumulates before localization occurs to form a “crack”. When the sample exhibits less spatial fluctuations, a non-negligible portion of the energy is dissipated into the matrix in the form of diffuse damage, resulting in fewer cracks and larger fragment sizes. As the normalized correlation gets even larger, i.e. Figures 4.14m to 4.14o, morphologically different crack networks are obtained.

On the other hand, the rougher samples generated using the PE covariance function, i.e. Figures 4.14d to 4.14f, 4.14j to 4.14l and 4.14p to 4.14r, have sufficient variations that serve as effective imperfections for damage localization. In terms of the mean size of fragments that form, the corresponding damage fields are seen to be far less sensitive to the spatial correlation length. However, as the correlation length increases, the orientation of the damage fields begins to acquire a structure that aligns with the axes of the domain. This observation is in accordance with the tensor-product structure of the covariance model, and with the fact that larger correlation lengths allow more pronounced spatial structures to develop (sample-wise) for PE functions.

Samples obtained with the two covariance models (parameterized by the same correlation lengths), considering the same realization for the underlying Gaussian field (from one covariance model to another), are compared in Figure 4.15 to study the effect of smoothness. It is seen that rougher material properties provide more candidate locations for damage localization, hence resulting in more fragments per unit volume of the domain (in a statistical sense). More precisely, the probability density functions (PDFs) corresponding to the dimensionless crack spacing (Figure 4.17),

estimated using approximately 2000 fragments and 10 independent realizations of the fields, show a substantial difference: the mean fragment size obtained with rough material properties (here, with the PE model) turns out to be much smaller than the mean fragment size generated by smoother samples of fracture properties (associated with the PSE model).

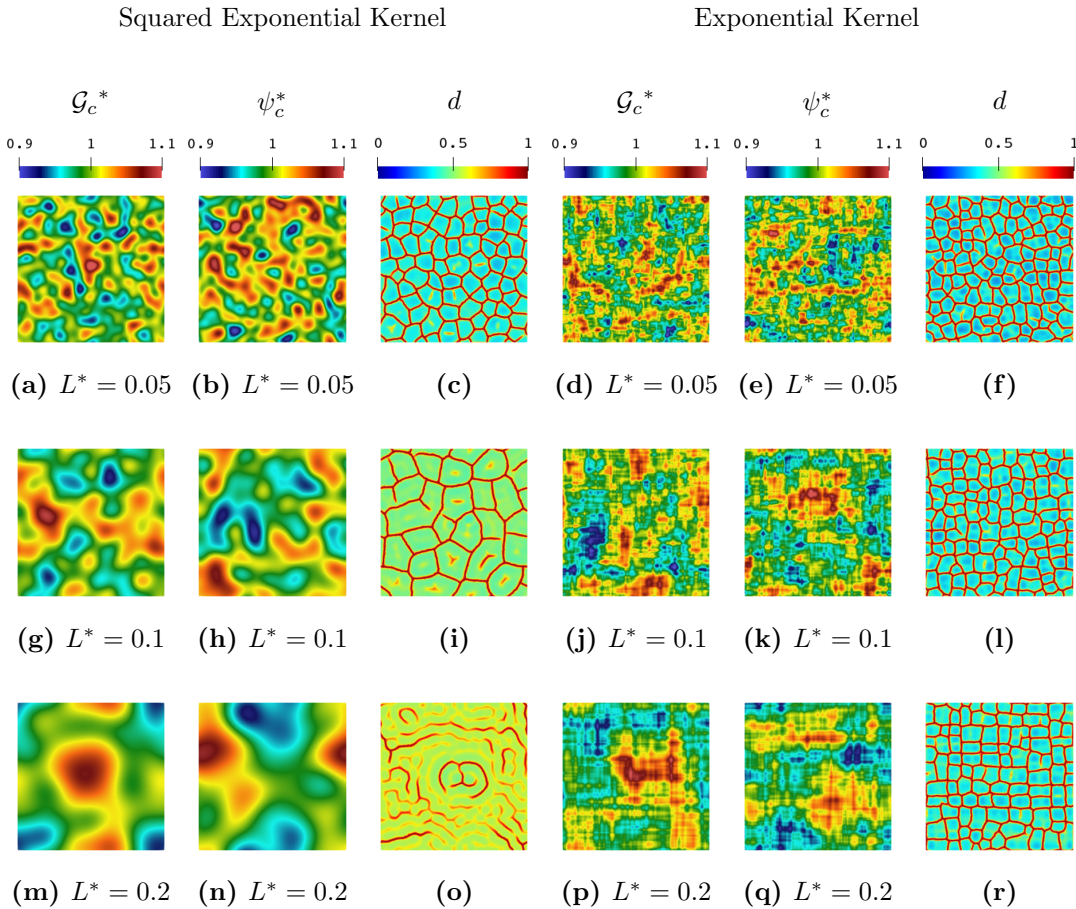


FIGURE 4.14. Damage fields resulting from six pairs of realizations with different correlation models and normalized correlation lengths. The left three pairs (a-b, g-h, m-n) are realizations obtained with a PSE covariance function, while the right three pairs (d-e, j-k, p-q) are samples generated with a PE covariance function. Energy release rate \mathcal{G}_c and the critical fracture energy ψ_c have a coefficient of variation of 0.03, and normalized spatial correlation length L^* of (a-b, d-e) 0.05 (g-h, j-k) 0.1 (m-n, p-q) 0.2. The corresponding damage fields are shown in (c, f, i, l, o, r), respectively. In these results, independent realizations of the underlying Gaussian fields are used.

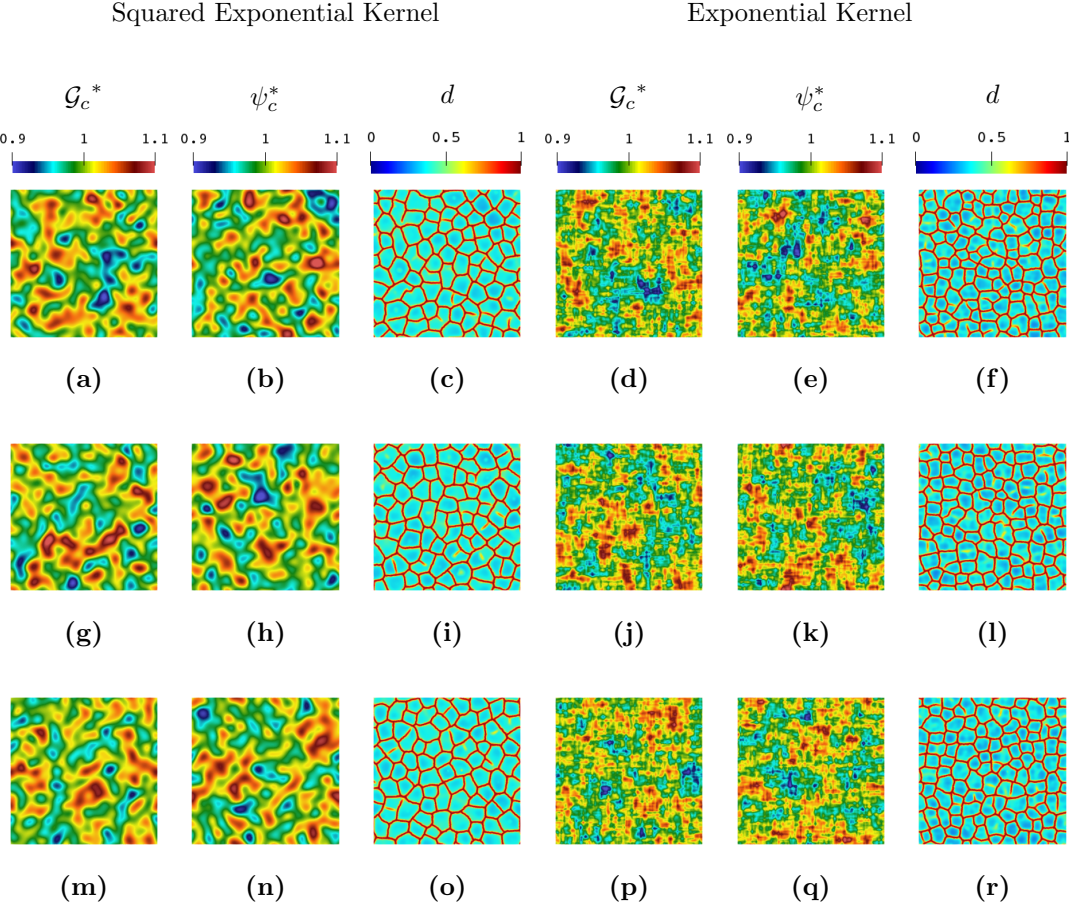


FIGURE 4.15. Three pairs of qualitative comparison of smoothness of the kernel function with the same normalized correlation length $L^* = 0.05$. (a-f) pair 1 (g-l) pair 2 (m-r) pair 3. Each row compares two kernel functions transformed from the same samples of the underlying Gaussian fields.

Parametric Analysis

The stochastic model constructed in this paper enables the introduction of point-wise correlation (that is, in the first-order marginal probability distribution) between the two fracture properties. With regard to fracture mechanics, one might wonder, for example, whether or not the fracture toughness \mathcal{G}_c and the critical fracture energy ψ_c are correlated (at a given location), and if so, to what extent. In this section, we perform a parametric analysis for different values of the correlation coefficient ρ ,

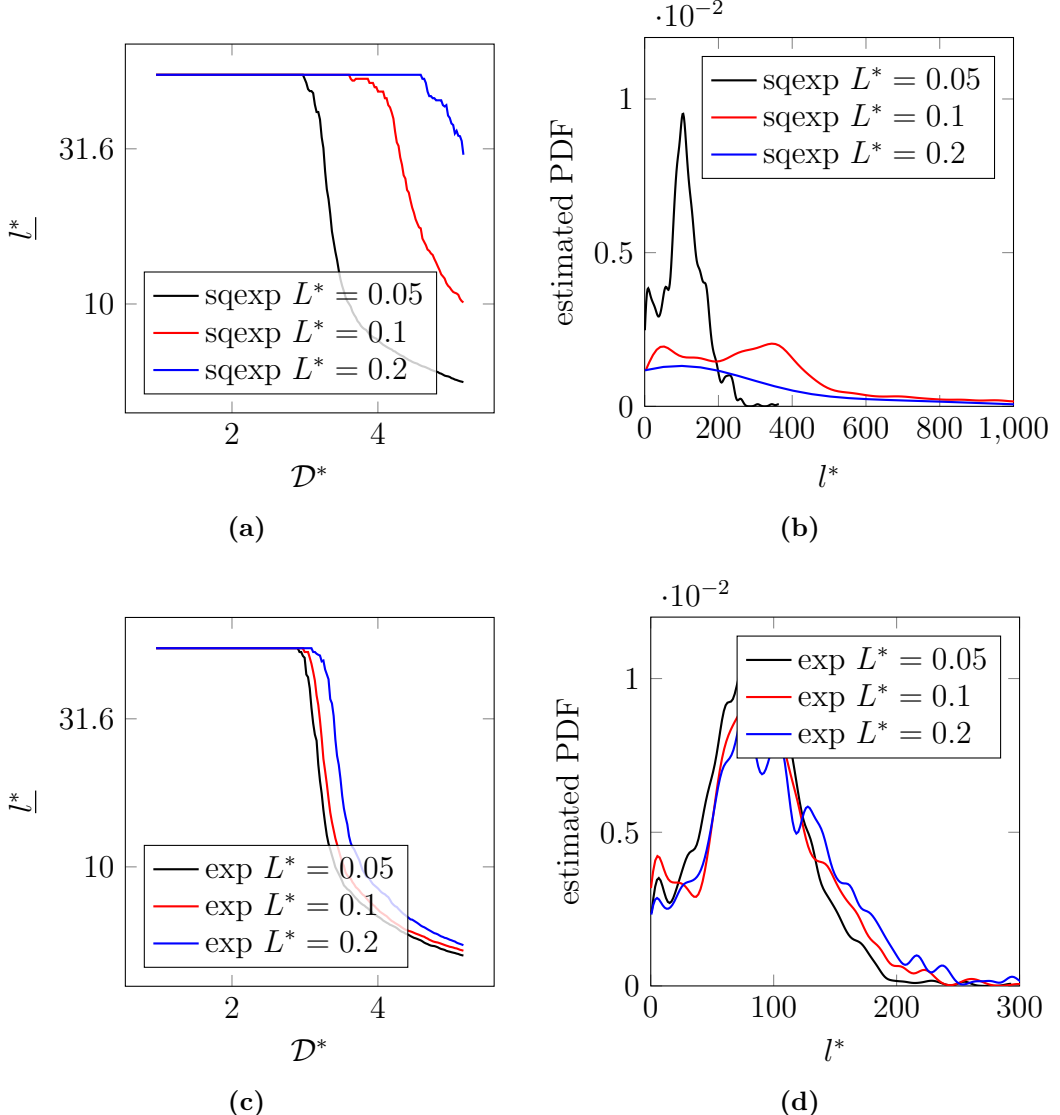


FIGURE 4.16. (a, c) Mean dimensionless crack spacing \underline{l}^* versus dimensionless crack driving force D^* (b, d) Estimated probability density of dimensionless crack spacing for different values of correlation length when $D^* = 5.17$ based on (a-b) a PSE kernel (c-d) a PE kernel

with the aim of understanding which field plays a dominant role in determining the resulting fracture morphology in thin films.

In order to obtain meaningful statistical results, 10 independent realizations are considered, and the same samples (of the underlying Gaussian random fields) are used when ρ varies. The normalized correlation length is set to $L^* = 0.05$ for

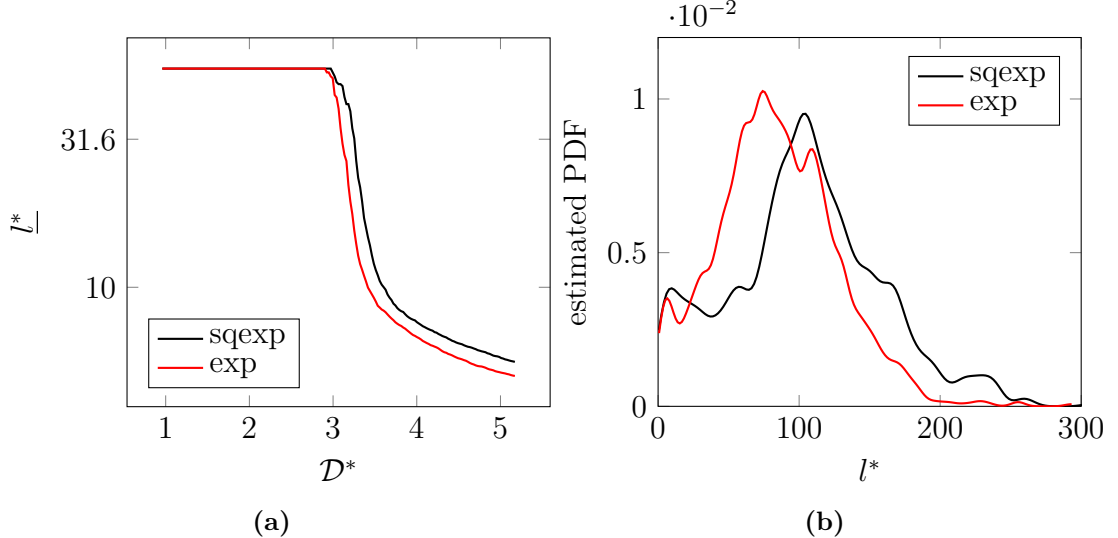


FIGURE 4.17. Comparisons of (a) mean dimensionless crack spacing \underline{l}^* versus dimensionless crack driving force D^* and (b) Estimated probability density of dimensionless crack spacing for different values of correlation length when $D^* = 5.17$ for results obtained using a PSE kernel and a PE kernel

both fracture properties. Three pairs of fracture toughness and critical fracture energy samples, constructed using (4.34) and (4.35) with $\rho \in \{0, 0.5, 1\}$, are shown in Figure 4.18. Note that the special case of $\rho = 0$ recovers the case of independent material properties.

Statistics of the dimensionless crack spacing \underline{l}^* are once again extracted at $D^* = 5.17$. The resulting dimensionless curves and normalized probability density functions are shown in Figures 4.19 and 4.20. These results indicate that the distribution of fragment size is relatively insensitive to the coefficient of correlation, regardless of the smoothness of the covariance kernel.

In contrast, when we superimpose the fracture patterns, we observe that the fracture morphology does exhibit a sensitivity to variations in the fracture toughness (Figure 4.21a). The superimposed results are only shown for the PSE covariance function, but comparable results are obtained with the PE covariance function. By comparison, when the fracture toughness is held fixed while the critical fracture

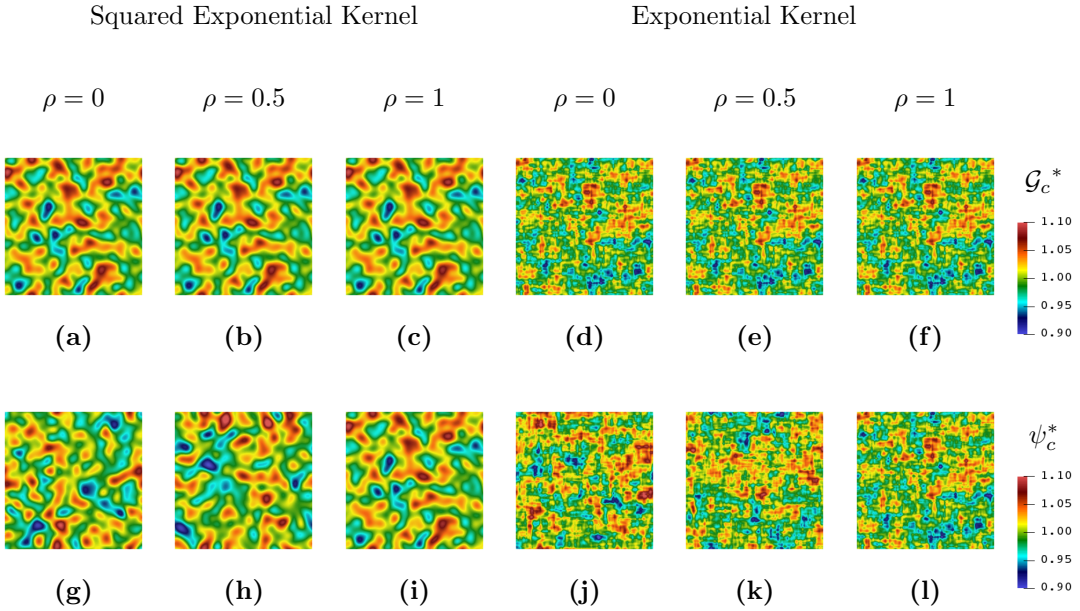


FIGURE 4.18. Point-wise correlated material properties: (a-f) normalized fracture toughness \mathcal{G}_c^* and (g-l) normalized critical fracture energy ψ_c^* with (left) PSE covariance function (right) PE covariance function

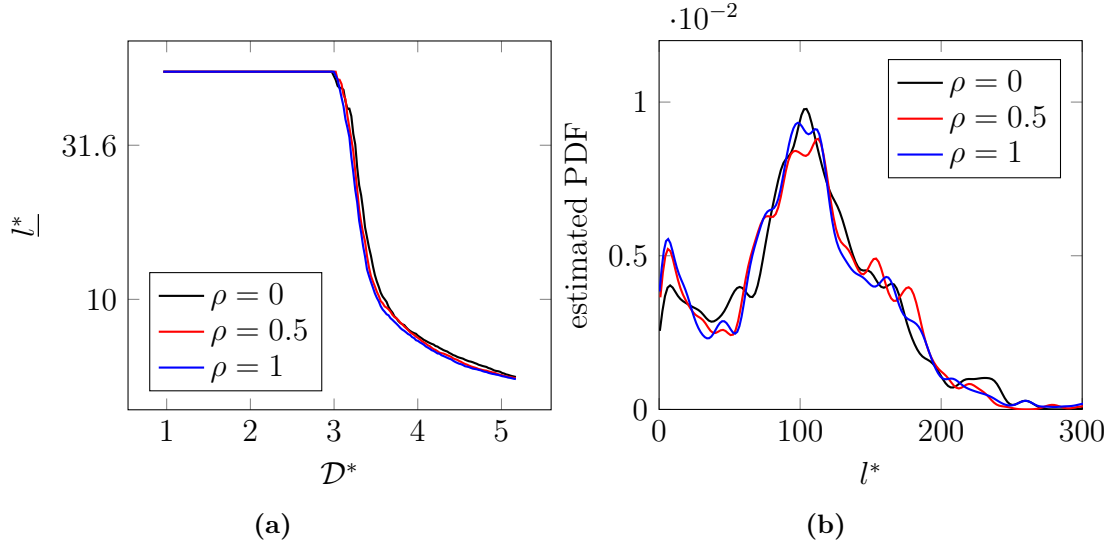


FIGURE 4.19. Comparisons of (a) mean dimensionless crack spacing as a function of dimensionless crack driving force and (b) estimated PDFs of dimensionless fragment size at loading $\mathcal{D}^* = 5.17$ for results with an underlying PSE kernel

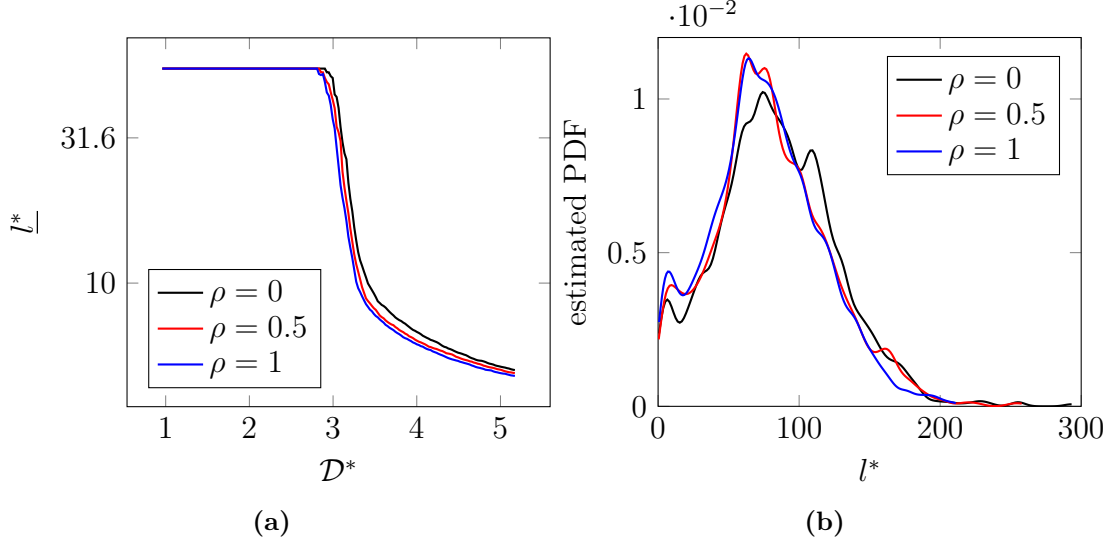


FIGURE 4.20. Comparisons of (a) mean dimensionless crack spacing and dimensionless crack driving force and (b) estimated PDFs of dimensionless fragment size at loading $D^* = 5.17$ for results with an underlying PE kernel

energy is varied, the superimposed fracture patterns are nearly indistinguishable (Figure 4.21b). The clear conclusion is that the energetics are primarily responsible for driving the fracture morphology, a result that is not surprising. This conclusion is also supported by the results shown in Figures 4.22 and 4.23, in which fracture patterns are plotted over contours of the fracture toughness and the critical energy. For both types of covariance functions, the fracture patterns are seen to follow contours of minimal fracture toughness while largely ignoring those of the critical fracture energy.

Discussion on Modeling Flexibility: Impact of the Covariance Structure

We now briefly examine how different structures of the covariance kernel can alter the fragment morphology. It has been demonstrated experimentally [41, 42, 43, 44, 45] how macro-scale processing conditions to construct samples may lead to morphologically different crack networks. For example, Kitsunezaki et al. [44] carried out a series of tests to study the effect of macroscopic disturbances on crack patterns.

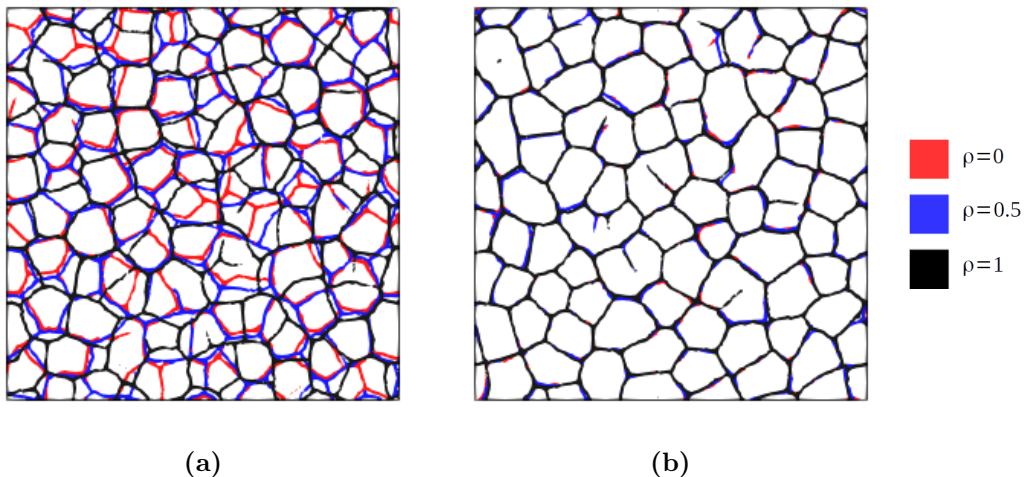


FIGURE 4.21. Superposition of fracture networks obtained by three samples of different coefficients of correlation, using the PSE kernel. Only the volume within the damage contour of $d = 0.9$ is shown to represent the resulting fracture network. Three samples are sampled (a) by holding \mathcal{G}_c constant and (b) by holding ψ_c constant.

They poured calcium carbonate (CaCO_3) paste into a shallow circular container. Different modes of agitation were applied to the paste before it was dried, and the resulting crack patterns showed a strong correlation with the modes of agitation.

We hypothesize that the agitation gives rise to effective fracture properties at the macro-scale that have a structure that is consistent with the agitation. We further assume a rougher spatial variation of properties in the direction parallel to the agitation than in the direction orthogonal to the agitation. Accordingly, we model the spatial variations in the fracture properties using composite covariance functions, defined on purpose by a tensor-product structure involving PSE and PE functions. In Figure 4.24, we compare the experimentally-observed crack patterns to our simulation results obtained using random fracture properties with the postulated anisotropic covariance functions. The comparison shows reasonable agreement (without specifically optimizing the hyperparameters in the stochastic model), indicating that the differing processing conditions may have resulted in different spatial

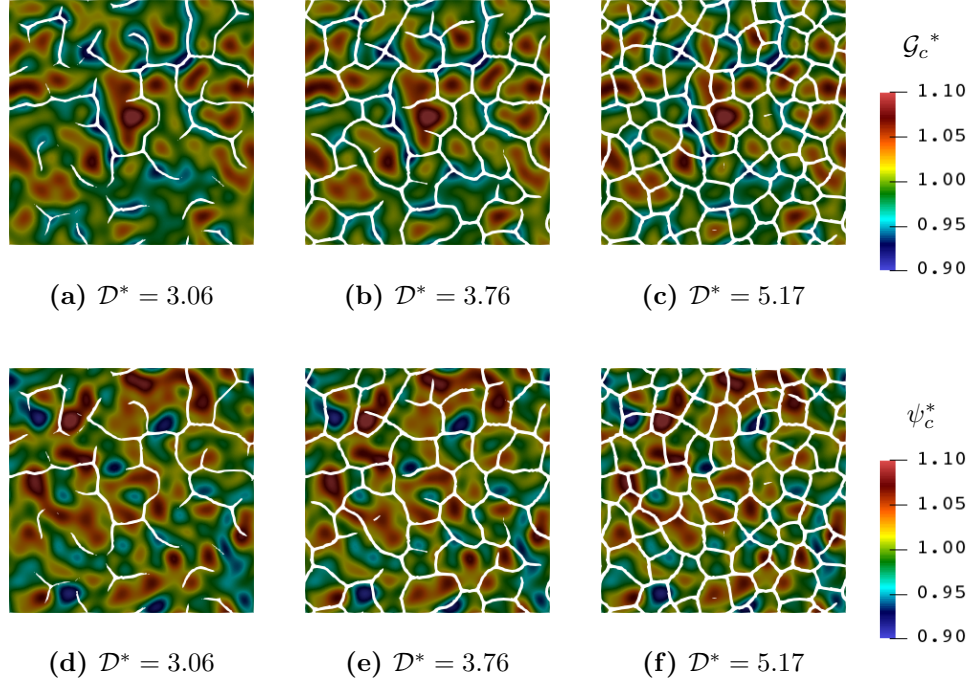


FIGURE 4.22. Snapshots of damage field at different loading levels with $d \geq 0.75$ plotted over (a-c) fracture toughness \mathcal{G}_c and (d-f) critical fracture energy ψ_c with an underlying PSE covariance function

variations in the effective fracture properties.

4.4.3 Inverse Identification Based on Three-Dimensional Physical Experiments

In Rodriguez [1], a series of drying tests with mining waste placed on grooved circular plates (225 mm in diameter) was performed to observe crack evolution due to desiccation processes. Three tests were carried out with different film thicknesses $h \in \{4 \text{ mm}, 8 \text{ mm}, \text{ and } 16 \text{ mm}\}$.

To replicate this study using model-based simulations and our phase-field model (enhanced with the stochastic description of fracture properties), we adopt fully three-dimensional models. The material properties used for this study are listed in Table 4.2. Consistent with the experimental studies of [1], the film-substrate system is represented by a cylindrical domain. The substrate is modeled as a rigid body

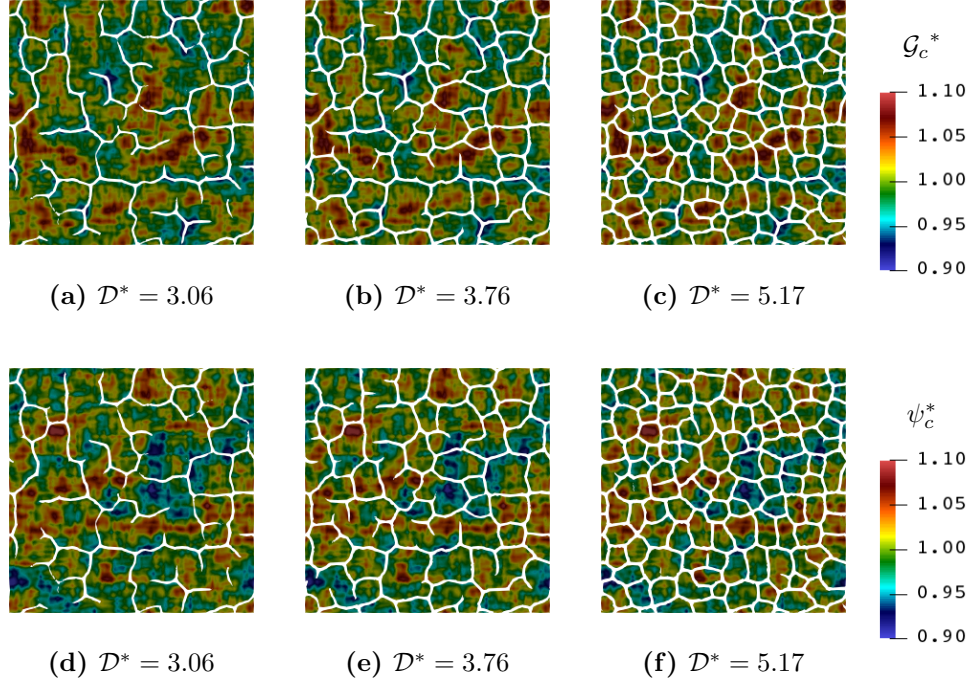


FIGURE 4.23. Snapshots of damage field at different loading levels with $d \geq 0.75$ plotted over (a-c) fracture toughness \mathcal{G}_c and (d-f) critical fracture energy ψ_c with an underlying PE covariance function

Table 4.2. Summary of material properties of mining waste and model parameters for all calculations in ??

Property/Parameter	Symbol	Value	Unit	Comment
Young's modulus	E	4	MPa	See [35]
Poisson's ratio	ν	0.2	nondim.	See [35]
Mean fracture toughness	$\underline{\mathcal{G}}_c$	27	kJ m^{-2}	See [66, 67]
Mean critical fracture energy	$\underline{\psi}_c$	30	J m^{-2}	See [66, 67]
Regularization length	l	0.8	mm	Such that $2l/h^e \approx 5$
Degradation shape parameter	p	1	nondim.	

with an arbitrarily high fracture toughness. The substrate and film are discretized using tetrahedral elements with characteristic lengths of $h_0^e = 1.6$ mm and $h_1^e = 0.36$ mm, respectively. The solutions to the linear elasticity subproblem, the phase-field for fracture subproblem, and the generalized eigenvalue problem are once again

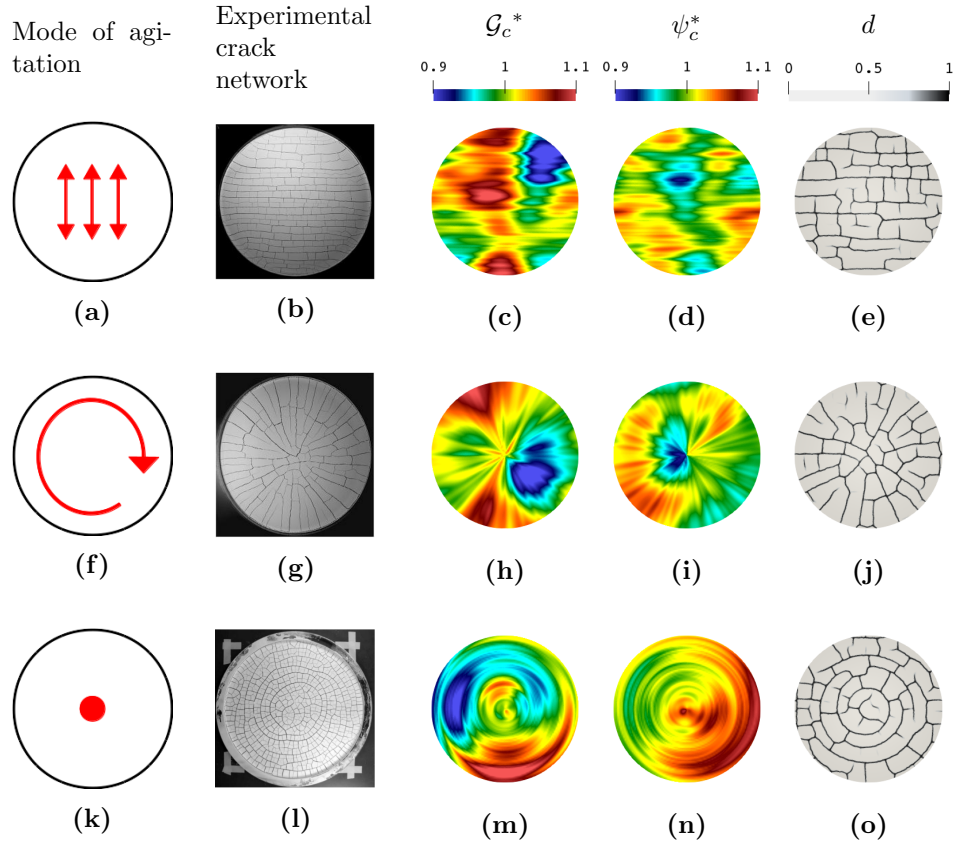


FIGURE 4.24. Three sets of experiments and calculations for (a-e) unilateral agitation (f-j) rotational agitation (k-o) point agitation. (b, g, l) snapshots of crack patterns from experiments. postulated spatially correlated (c, h, m) fracture toughness and (d, i, n) critical fracture energy to reproduce experimental observations. (e, j, o) damage fields obtained using corresponding spatially varying material properties.

approximated using the same mesh.

We first calibrate the spatial variability in our model against the experimental observations of the fracture patterns for the thinnest ($h = 4\text{mm}$) specimen. To formulate the statistical inverse problem, we assume that (1) the fracture toughness and the critical fracture energy are uncorrelated (i.e., $\rho = 0$); and (2) both fracture properties have the same coefficient of variation (set to 0.03) and spatial correlation lengths, and that they can be defined using isotropic squared exponential kernels.

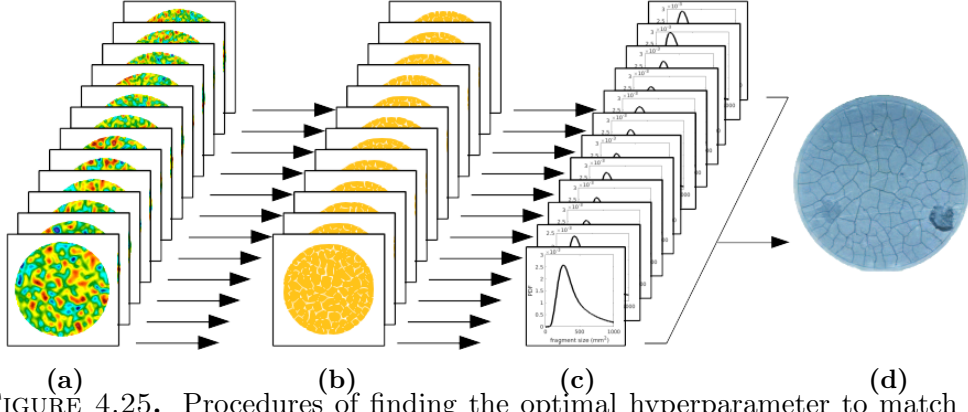


FIGURE 4.25. Procedures of finding the optimal hyperparameter to match the experiment: (a) 12 pairs of fracture properties are sampled to explore the space of admissible spatial correlation lengths; three dimensional energy minimization problems are solved to obtain (b) the resulting fracture morphology; (c) distributions of fragment sizes are extracted from the simulated results, and the log-likelihood values of these distributions at the samples extracted from (d) the experimental fracture morphology are computed.

In addition, the variations of the properties through the thickness of the film are assumed negligible compared to in-plane variations.

Based on these assumptions, the spatial correlation length L is the only parameter to be determined, and a parametric search is performed in $\mathbb{L} = \{ 3 \text{ mm}, 3.5 \text{ mm}, 4 \text{ mm}, 4.5 \text{ mm}, 5 \text{ mm}, 5.5 \text{ mm}, 6 \text{ mm}, 6.5 \text{ mm}, 7 \text{ mm}, 7.5 \text{ mm}, 8 \text{ mm}, 8.5 \text{ mm} \}$. Energy minimization problems for the case of $h = 4 \text{ mm}$ are simulated for each pair of realizations and the corresponding fracture patterns are obtained. For a given value of $L \in \mathbb{L}$, the flooding algorithm is used to identify fragments on the top surface of the thin film, and a kernel density estimation of the probability density function associated with the fragment size, denoted by $f_{\text{fs}}^{\text{sim}}(\cdot; L)$, is obtained. The optimal value of L is then identified by maximizing the log-likelihood function \mathcal{L} defined as

$$\mathcal{L}(L) = \sum_{A_{\text{fs}}^{\text{exp}} \in \mathbb{A}_{\text{exp}}} \ln f_{\text{fs}}^{\text{sim}}(l^*(A_{\text{fs}}^{\text{exp}}); L), \quad l^*(A) = \frac{\sqrt{A}}{h}, \quad (4.77)$$

where \mathbb{A}_{exp} denotes the collection of fragment size samples extracted by using the same flooding algorithm on the experimental result. The aforementioned workflow

to calibrate the model is summarized in Figure 4.25. The fracture properties with spatial correlation $L = 4$ mm lead to the maximum log-likelihood among the span of samples considered. Figure 4.26 compares the estimated PDF and the fracture morphology obtained using the calibrated stochastic model to those of the experimental specimen for $h = 4$ mm.

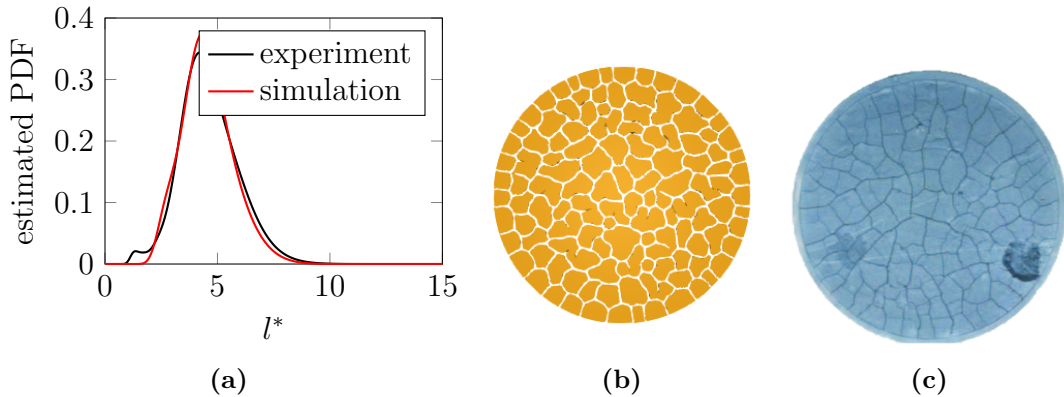


FIGURE 4.26. (a) Estimated PDFs of the dimensionless fragment sizes extracted from the experimental result and the calibrated stochastic model. (b) Fracture morphology obtained using the calibrated fracture properties. (c) Photograph of cracks in the mining waste.

To then benchmark our model against specimens with different thicknesses, three 3D calculations are carried out using the same realization of fracture properties with $L = 4$ mm. As shown in Figure 4.27, our results appear to agree reasonably well with the experimental observations. In general, the thicker films fracture into larger fragments, which also agrees with the simplified models presented in ????.

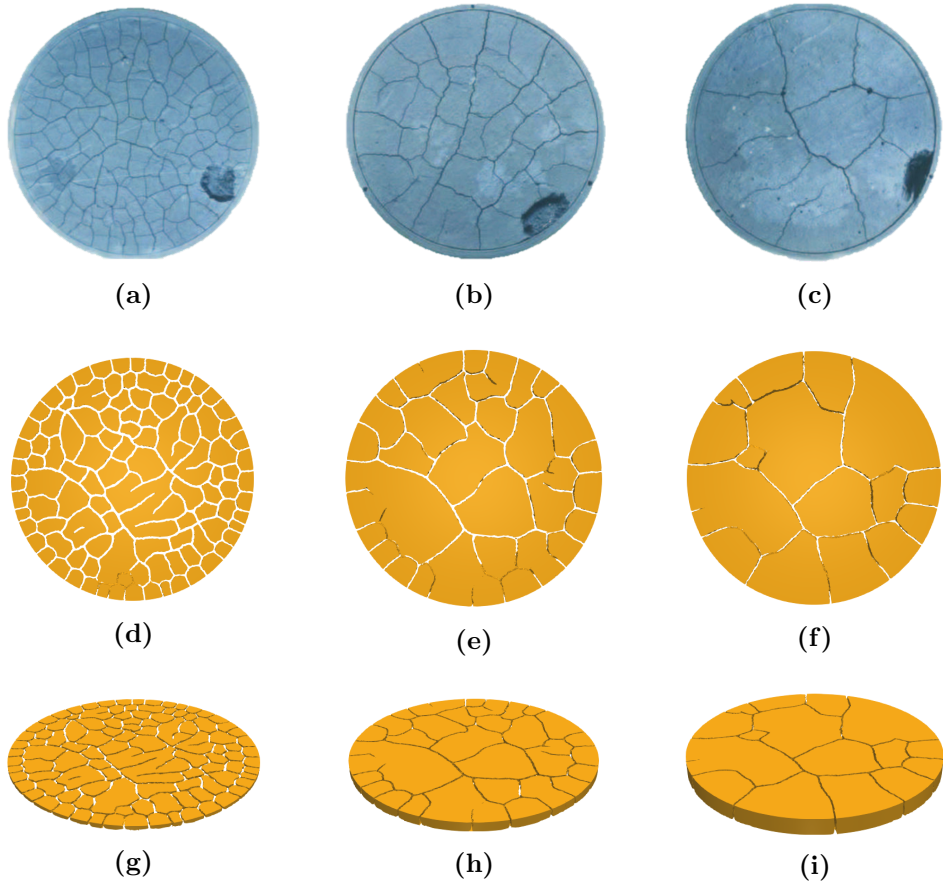


FIGURE 4.27. Qualitative comparison between the experiments and the simulations: (a-c) Photographs (modified from [1]) of cracks in mining waste due to desiccation at steady state for three test specimens with thickness (a) 4 mm, (b) 8 mm, and (c) 16 mm. (d-f) Top view and (g-i) panoramic view of corresponding numerical simulation results with different film thickness. Volumes of material with $d \geq 0.75$ were removed to improve the visualization of the crack geometry.

5

Towards Ductile Fracture

5.1 Introduction

5.2 Theory

5.2.1 *Constitutive choices*

5.2.2 *A power-law approximation to the yield surface*

5.2.3 *Variational constitutive updates*

5.3 Verification

5.3.1 *A homogeneous example: uniaxial constitutive response*

5.3.2 *A nonhomogeneous example: uniaxial load-displacement curves*

5.3.3 *Crack resistance curves*

5.4 Numerical examples

5.4.1 *Three-point bending*

5.4.2 *The Sandia Fracture Challenge*

5.4.3 *Spallation of oxidation scale*

6

Conclusion

Appendix A

Code availability

Appendix B

On the phase-field irreversibility constraint

Appendix C

The flooding algorithm for counting fragments

We describe the algorithm for clustering various elements in a mesh to individual fragments, as delineated by a damage field. The algorithm assigns each element a cluster order parameter, and different clusters are separated by a band of “broken” elements where the damage is above a threshold, i.e. $d > d_{\text{th}}$. Figure C.1 provides an example of this algorithm for a representative damage field.

The algorithm has a fundamental “flooding” structure. In particular, a seeding element broadcasts its information to all of its geometric neighbors, and each neighbor becomes a new seed for the next round of information propagation. In the context of counting fragments, the information of an element includes its state and the cluster it belongs to. An element is considered to be “intact” if all of its nodal damage values are below d_{th} , otherwise it is considered to be “broken”.

Three lists are managed by the algorithm. The first list **ALL** includes all elements that need to be classified. The second list **CANDIDATE**, optionally a first-in-first-out (FIFO) queue, includes all candidate elements for the current cluster. The third list **BROKEN** includes all “broken” elements. Each cluster CLUSTER^i is essentially a list of

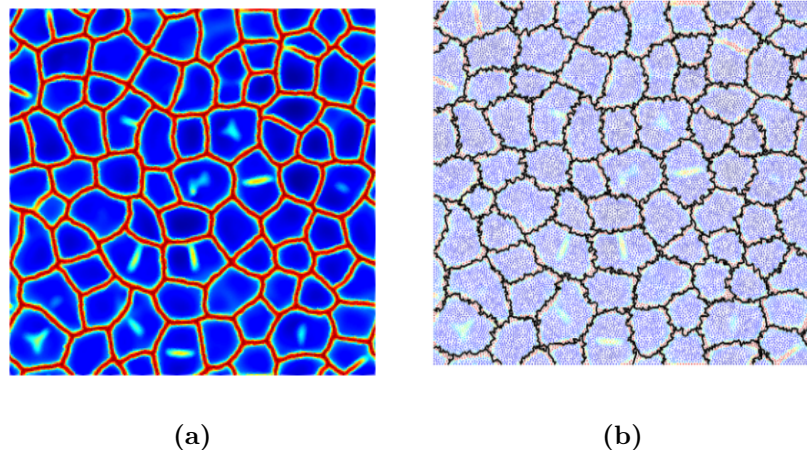


FIGURE C.1. (a) Final damage field obtained using a spatially correlated random \mathcal{G}_c and ψ_c . (b) Corresponding clusters labeled by the flooding algorithm. Cluster boundaries are marked in black.

elements that belong to the same parent cluster.

The algorithm consists of three stages. In the first stage, we update the damage values of all nodes and states of all elements. All elements that have a status change require reclassification. Therefore, any cluster that contains elements pending reclassification is pushed into **ALL** for future reclassification.

In the second stage, all “intact” elements in **ALL** are pushed into **CANDIDATE** one at a time until **ALL** has no more “intact” elements. Each new cluster is constructed by dequeuing **CANDIDATE**. The first element in **CANDIDATE** is dequeued after all of its connecting “intact” elements from **ALL** are pushed into **CANDIDATE**.

During the third stage, “broken” elements are grouped into their nearest cluster to preserve the total volume of the mesh. In our implementation, “broken” elements are assigned to clusters based on the solution to a minimization problem of weighted Euclidean distance between the elements and cluster centroids.

The skeleton of the flooding algorithm is outlined in Algorithm 1.

Algorithm 1 An iterative flooding algorithm for fragmentation count

```
1: Set  $d_0 \leftarrow 0$ 
2: Set cluster count  $c \leftarrow 0$ 
3: Group all elements into  $\text{CLUSTER}^c$ 
4: for time step  $n \in \{0, 1, 2, \dots\}$  do
5:   for each cluster  $\text{CLUSTER}^i$  do
6:     Move all “broken” elements into  $\text{BROKEN}$ 
7:     if  $\text{CLUSTER}^i$  contains any element that has a state change, i.e. from “intact” to “broken” then
8:       Move all remaining elements into  $\text{ALL}$ 
9:     end if
10:    end for
11:    while  $\text{ALL}$  is not empty do
12:      if All elements in  $\text{ALL}$  are “broken” then
13:        Move all elements in  $\text{ALL}$  into  $\text{BROKEN}$ 
14:        Break while loop
15:      else
16:        Move one “intact” element from  $\text{ALL}$  to  $\text{CANDIDATE}$ 
17:        Increment cluster count  $c \leftarrow c + 1$ 
18:        while  $\text{ALL}$  is not empty do
19:          for each element  $e$  that shares a common edge with the first element
in the queue  $\text{CANDIDATE}$  do
20:            if  $e$  is “intact” then
21:              Enqueue  $e$  into  $\text{CANDIDATE}$ 
22:            else
23:              Move  $e$  into  $\text{BROKEN}$ 
24:            end if
25:          end for
26:          Dequeue first element in  $\text{CANDIDATE}$  into  $\text{CLUSTER}^c$ 
27:        end while
28:      end if
29:    end while
30:    Move all elements in  $\text{BROKEN}$  into their nearest cluster
31: end for
```

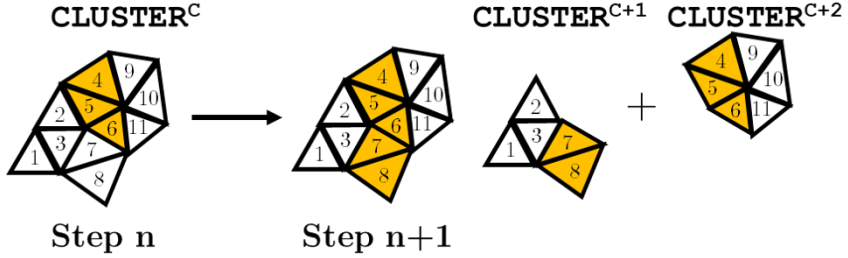


FIGURE C.2. Status change from step n to step $n+1$. “Broken” elements are labeled in yellow, and “intact” elements are white. The step-by-step reclassification procedure is shown in Table C.1.

Table C.1. Demonstration of classification after the update from time step n to time step $n+1$. Broken elements are denoted with an underscore.

Step	Stage	ALL	CANDIDATE	BROKEN	Comments
n		\emptyset	\emptyset	\emptyset	$\text{CLUSTER}^c = \{1, 2, 3, \underline{4}, \underline{5}, \underline{6}, 7, 8, 9, 10, 11\}$
$n+1$		\emptyset	\emptyset	\emptyset	$\text{CLUSTER}^c = \{1, 2, 3, \underline{4}, \underline{5}, \underline{6}, \underline{7}, \underline{8}, 9, 10, 11\}$
$n+1$	1	$\{1, 2, 3, 9, 10, 11\}$	\emptyset	$\{\underline{4}, \underline{5}, \underline{6}, \underline{7}, \underline{8}\}$	Declassify CLUSTER^c
$n+1$	2	$\{2, 3, 9, 10, 11\}$	$\{1\}$	$\{\underline{4}, \underline{5}, \underline{6}, \underline{7}, \underline{8}\}$	Enqueue element 1 to CANDIDATE
$n+1$	2	$\{9, 10, 11\}$	$\{1, 2, 3\}$	$\{\underline{4}, \underline{5}, \underline{6}, \underline{7}, \underline{8}\}$	Enqueue connected elements 2, 3
$n+1$	2	$\{9, 10, 11\}$	$\{2, 3\}$	$\{\underline{4}, \underline{5}, \underline{6}, \underline{7}, \underline{8}\}$	Dequeue element 1
$n+1$	2	$\{9, 10, 11\}$	$\{3\}$	$\{\underline{4}, \underline{5}, \underline{6}, \underline{7}, \underline{8}\}$	Dequeue element 2
$n+1$	2	$\{9, 10, 11\}$	\emptyset	$\{\underline{4}, \underline{5}, \underline{6}, \underline{7}, \underline{8}\}$	Dequeue element 3
$n+1$	2	$\{10, 11\}$	$\{9\}$	$\{\underline{4}, \underline{5}, \underline{6}, \underline{7}, \underline{8}\}$	$\text{CLUSTER}^{c+1} = \{1, 2, 3\}$
$n+1$	2	\emptyset	$\{9, 10, 11\}$	$\{\underline{4}, \underline{5}, \underline{6}, \underline{7}, \underline{8}\}$	Enqueue element 9 to CANDIDATE
$n+1$	2	\emptyset	$\{10, 11\}$	$\{\underline{4}, \underline{5}, \underline{6}, \underline{7}, \underline{8}\}$	Enqueue connected elements 10, 11
$n+1$	2	\emptyset	$\{11\}$	$\{\underline{4}, \underline{5}, \underline{6}, \underline{7}, \underline{8}\}$	Dequeue element 9
$n+1$	2	\emptyset	\emptyset	$\{\underline{4}, \underline{5}, \underline{6}, \underline{7}, \underline{8}\}$	Dequeue element 10
$n+1$	2	\emptyset	\emptyset	$\{\underline{4}, \underline{5}, \underline{6}, \underline{7}, \underline{8}\}$	Dequeue element 11
$n+1$	3	\emptyset	\emptyset	$\{\underline{4}, \underline{5}, \underline{6}\}$	Group elements 7, 8 into CLUSTER^{c+1}
$n+1$	3	\emptyset	\emptyset	\emptyset	Group elements 4, 5, 6 into CLUSTER^{c+2}

Bibliography

- [1] R Rodriguez. Hydrogeotechnical characterization of a metallurgical waste. *Canadian Geotechnical Journal*, 43(10):1042–1060, 2006.
- [2] G.A. Francfort and J.J. Marigo. Revisiting brittle fracture as an energy minimization problem. *Journal of the Mechanics and Physics of Solids*, 46(8):1319–1342, 1998.
- [3] B. Bourdin, G.A. Francfort, and J.J. Marigo. Numerical experiments in revisited brittle fracture. *Journal of the Mechanics and Physics of Solids*, 48(4):797–826, 2000.
- [4] Blaise Bourdin, Gilles A Francfort, and Jean-Jacques Marigo. The variational approach to fracture. *Journal of elasticity*, 91(1-3):5–148, 2008.
- [5] A. Karma, D. A. Kessler, and H. Levine. Phase-field model of mode III dynamic fracture. *Physical Review Letters*, 87(4):045501–1–4, 2001.
- [6] A. Karma and A. E. Lobkovsky. Unsteady crack motion and branching in a phase-field model of brittle fracture. *Physical Review Letters*, 93(10):245510, 2004.
- [7] H. Henry and H. Levine. Dynamic instabilities of fracture under biaxial strain using a phase field model. *Physical Review Letters*, 93(10):105504, 2004.
- [8] R. Spatschek, C. M. Gugenberger, and E. Brener. Phase field modeling of fracture and stress-induced phase transitions. *Physical Review E*, 75:066111, 2007.
- [9] H. Amor, J. J. Marigo, and C. Maurini. Regularized formulation of the variational brittle fracture with unilateral contact: Numerical experiments. *Journal of the Mechanics and Physics of Solids*, 57(8):1209–1229, 2009.
- [10] AAL Baldelli, B Bourdin, JJ Marigo, and C Maurini. Delamination and fracture of thin films: a variational approach. *Direct and variational methods for nonsmooth problems in mechanics Amboise, France*, 2013.

- [11] AA León Baldelli, J-F Babadjian, Blaise Bourdin, Duvan Henao, and Corrado Maurini. A variational model for fracture and debonding of thin films under in-plane loadings. *Journal of the Mechanics and Physics of Solids*, 70:320–348, 2014.
- [12] C. Miehe, F. Welschinger, and M. Hofacker. Thermodynamically consistent phase-field models of fracture: Variational principles and multi-field FE implementations. *International Journal for Numerical Methods in Engineering*, 83: 1273–1311, 2010.
- [13] C. Miehe, M. Hofacker, and F. Welschinger. A phase field model for rate-independent crack propagation: Robust algorithmic implementation based on operator splits. *Computer Methods in Applied Mechanics and Engineering*, 199: 2765–2778, 2010.
- [14] Hanen Amor, Jean-Jacques Marigo, and Corrado Maurini. Regularized formulation of the variational brittle fracture with unilateral contact: Numerical experiments. *Journal of the Mechanics and Physics of Solids*, 57(8):1209 – 1229, 2009. ISSN 0022-5096.
- [15] Michael Strobl and Thomas Seelig. A novel treatment of crack boundary conditions in phase field models of fracture. *Pamm*, 15(1):155–156, 2015.
- [16] Michael Strobl and Thomas Seelig. On constitutive assumptions in phase field approaches to brittle fracture. *Procedia Structural Integrity*, 2:3705–3712, 2016.
- [17] Fan Fei and Jinhyun Choo. A phase-field method for modeling cracks with frictional contact. *arXiv preprint arXiv:1905.10547*, 2019.
- [18] Fan Fei and Jinhyun Choo. A phase-field model of geologic shear fracture, 2020.
- [19] Yu-Sheng Lo, Michael Borden, K. Ravi-Chandar, and Chad M. Landis. A phase-field model for fatigue crack growth. *Journal of the Mechanics and Physics of Solids*, 132(103684), 2019.
- [20] JTA Roberts, E Smith, N Fuhrman, and D Cubicciotti. On the pellet-cladding interaction phenomenon. *Nuclear Technology*, 35(1):131–144, 1977.
- [21] Bruno Michel, Jérôme Sercombe, Gilles Thouvenin, and Rémy Chatelet. 3d fuel cracking modelling in pellet cladding mechanical interaction. *Engineering fracture mechanics*, 75(11):3581–3598, 2008.
- [22] Lars Olof Jernkvist. A model for predicting pellet-cladding interaction-induced fuel rod failure. *Nuclear engineering and design*, 156(3):393–399, 1995.

- [23] Fumihsa Nagase and Toyoshi Fuketa. Effect of pre-hydriding on thermal shock resistance of zircaloy-4 cladding under simulated loss-of-coolant accident conditions. *Journal of nuclear science and technology*, 41(7):723–730, 2004.
- [24] Michael Billone, Yong Yan, Tatiana Burtseva, Robert Daum, et al. Cladding embrittlement during postulated loss-of-coolant accidents. Technical report, Argonne National Lab.(ANL), Argonne, IL (United States), 2008.
- [25] Mohamed M El-Basyouny and Matthew Witczak. Calibration of alligator fatigue cracking model for 2002 design guide. *Transportation research record*, 1919(1):76–86, 2005.
- [26] Sherif M El-Badawy, Myung Goo Jeong, and Mohamed El-Basyouny. Methodology to predict alligator fatigue cracking distress based on asphalt concrete dynamic modulus. *Transportation Research Record*, 2095(1):115–124, 2009.
- [27] T Saar and O Talvik. Automatic asphalt pavement crack detection and classification using neural networks. In *2010 12th Biennial Baltic Electronics Conference*, pages 345–348. IEEE, 2010.
- [28] Joe W Button and Robert L Lytton. Guidelines for using geosynthetics with hot-mix asphalt overlays to reduce reflective cracking. *Transportation Research Record*, 2004(1):111–119, 2007.
- [29] Yetkin Yildirim, Ahmed Qatan, Jorge Prozzi, et al. *Field manual for crack sealing in asphalt pavements.*, 2006.
- [30] John W Hutchinson and Zhigang Suo. Mixed mode cracking in layered materials. In *Advances in applied mechanics*, volume 29, pages 63–191. Elsevier, 1991.
- [31] Kevin M Crosby and R Mark Bradley. Fragmentation of thin films bonded to solid substrates: Simulations and a mean-field theory. *Physical Review E*, 55(5):6084, 1997.
- [32] Kwan-tai Leung and Zoltan Néda. Pattern formation and selection in quasistatic fracture. *Physical review letters*, 85(3):662, 2000.
- [33] Supti Sadhukhan, Tapati Dutta, and Sujata Tarafdar. Crack formation in composites through a spring model. *Physica A: Statistical Mechanics and its Applications*, 390(4):731–740, 2011.
- [34] Jingwen Zhang, Yuyang Lu, Linghui He, Lizhong Yang, and Yong Ni. Modeling progressive interfacial debonding of a mud-crack film on elastic substrates. *Engineering Fracture Mechanics*, 177:123–132, 2017.

- [35] Marcelo Sánchez, Osvaldo L Manzoli, and Leonardo JN Guimarães. Modeling 3-d desiccation soil crack networks using a mesh fragmentation technique. *Computers and Geotechnics*, 62:27–39, 2014.
- [36] J Liang, R Huang, Jean-Herve Prevost, and Z Suo. Evolving crack patterns in thin films with the extended finite element method. *International Journal of Solids and Structures*, 40(10):2343–2354, 2003.
- [37] N Sukumar and J-H Prévost. Modeling quasi-static crack growth with the extended finite element method part i: Computer implementation. *International journal of solids and structures*, 40(26):7513–7537, 2003.
- [38] Rui Huang, N Sukumar, and J-H Prévost. Modeling quasi-static crack growth with the extended finite element method part ii: Numerical applications. *International Journal of Solids and Structures*, 40(26):7539–7552, 2003.
- [39] Z Cedric Xia and John W Hutchinson. Crack patterns in thin films. *Journal of the Mechanics and Physics of Solids*, 48(6-7):1107–1131, 2000.
- [40] HM Yin, GH Paulino, and William G Buttlar. An explicit elastic solution for a brittle film with periodic cracks. *International Journal of Fracture*, 153(1):39, 2008.
- [41] So Kitsunezaki, Akio Nakahara, and Yousuke Matsuo. Shaking-induced stress anisotropy in the memory effect of paste. *EPL (Europhysics Letters)*, 114(6):64002, 2016.
- [42] So Kitsunezaki, Yousuke Matsuo, and Akio Nakahara. Stress development up to crack formation in drying paste. *Journal of Chemical Engineering of Japan*, 50(10):775–779, 2017.
- [43] Zoltán Halász, Akio Nakahara, So Kitsunezaki, and Ferenc Kun. Effect of disorder on shrinkage-induced fragmentation of a thin brittle layer. *Physical Review E*, 96(3):033006, 2017.
- [44] So Kitsunezaki, Arina Sasaki, Akihiro Nishimoto, Tsuyoshi Mizuguchi, Yousuke Matsuo, and Akio Nakahara. Memory effect and anisotropy of particle arrangements in granular paste. *The European Physical Journal E*, 40(10):88, 2017.
- [45] Akio Nakahara, Tomoki Hiraoka, Rokuya Hayashi, Yousuke Matsuo, and So Kitsunezaki. Mechanism of memory effect of paste which dominates desiccation crack patterns. *Philosophical Transactions of the Royal Society A*, 377(2136):20170395, 2018.

- [46] Katherine A. Acton, Sarah C. Baxter, Bahador Bahmani, Philip L. Clarke, and Reza Abedi. Voronoi tessellation based statistical volume element characterization for use in fracture modeling. *Computer Methods in Applied Mechanics and Engineering*, 336:135 – 155, 2018.
- [47] Darith-Anthony Hun, Johann Guilleminot, Julien Yvonnet, and Michel Bornert. Stochastic multiscale modeling of crack propagation in random heterogeneous media. *International Journal for Numerical Methods in Engineering*, 119(13): 1325–1344, 2019.
- [48] C. Peco, Y. Liu, C. Rhea, and J.E. Dolbow. Models and simulations of surfactant-driven fracture in particle rafts. *International Journal of Solids and Structures*, 156:194–209, 2019.
- [49] Jian-Ying Wu and Miguel Cervera. A thermodynamically consistent plastic-damage framework for localized failure in quasi-brittle solids: Material model and strain localization analysis. *International Journal of Solids and Structures*, 88:227–247, 2016.
- [50] Jian-Ying Wu. A unified phase-field theory for the mechanics of damage and quasi-brittle failure. *Journal of the Mechanics and Physics of Solids*, 103:72–99, 2017.
- [51] Rudy JM Geelen, Yingjie Liu, Tianchen Hu, Michael R Tupek, and John E Dolbow. A phase-field formulation for dynamic cohesive fracture. *Computer Methods in Applied Mechanics and Engineering*, 348:680–711, 2019.
- [52] Eric Lorentz, Sam Cuvilliez, and Kyrylo Kazymyrenko. Convergence of a gradient damage model toward a cohesive zone model. *Comptes Rendus Mécanique*, 339(1):20–26, 2011.
- [53] Eric Lorentz. A nonlocal damage model for plain concrete consistent with cohesive fracture. *International Journal of Fracture*, 207(2):123–159, 2017.
- [54] Mircea Grigoriu. Existence and construction of translation models for stationary non-gaussian processes. *Probabilistic Engineering Mechanics*, 24:545–551, 2009.
- [55] E.T. Jaynes. Information theory and statistical mechanics i. *Physical Review*, 106(4):620–630, 1957.
- [56] E.T. Jaynes. Information theory and statistical mechanics ii. *Physical Review*, 108(2):171–190, 1957.
- [57] C.E. Shannon. A mathematical theory of communication. *Bell System Technical Journal*, 27(3):379–423, 1948.

- [58] C.E. Shannon. A mathematical theory of communication. *Bell System Technical Journal*, 27(4):623–656, 1948.
- [59] N. Balakrishnan and C.-D. Lai. *Continuous Bivariate Distributions*. Springer-Verlag New York, 2009.
- [60] Patrick Moran. Statistical inference with bivariate gamma distributions. *Biometrika Trust*, 56:627–634, 1969.
- [61] R. G. Ghanem and P. D. Spanos. *Stochastic Finite Elements: A Spectral Approach (Revised Edition)*. Dover, 2003.
- [62] O. Le Maître and O. Knio. *Spectral Methods for Uncertainty Quantification*. Springer Netherlands, 2010.
- [63] J.L. Beuth. Cracking of thin bonded films in residual tension. *International Journal of Solids and Structures*, 29(13):1657 – 1675, 1992. ISSN 0020-7683.
- [64] R Obrzud. *The hardening soil model: A practical guidebook*. Zace Services, 2010.
- [65] A Ramsaroop, K Kanny, and TP Mohan. Fracture toughness studies of polypropylene-clay nanocomposites and glass fibre reinforced polypropylene composites. *Materials Sciences and Applications*, 1(05):301, 2010.
- [66] R Rodríguez, Marcelo Sanchez, A Ledesma, and A Lloret. Experimental and numerical analysis of desiccation of a mining waste. *Canadian Geotechnical Journal*, 44(6):644–658, 2007.
- [67] MR Lakshmikantha, PC Prat, and A Ledesma. Image analysis for the quantification of a developing crack network on a drying soil. *Geotechnical Testing Journal*, 32(6):505–515, 2009.

Biography

About myself.